




Article

A Numerical Investigation on the Aeroacoustic Noise Emission from Offshore Wind Turbine Wake Interference

Yan Yan , Lei Xue , Jundong Wang , Zhichao Yang  and Yu Xue * 

College of Engineering, Ocean University of China, Qingdao 266100, China; yy4961@stu.ouc.edu.cn (Y.Y.); xuelei@stu.ouc.edu.cn (L.X.); sakura_ouc@stu.ouc.edu.cn (J.W.); yangzhichao@stu.ouc.edu.cn (Z.Y.)

* Correspondence: xueyu7231@ouc.edu.cn

Abstract: Offshore wind turbine (WT) wake interference will reduce power generation and increase the fatigue loads of downstream WTs. Wake interference detection based on aeroacoustic noise is believed to solve these challenges in offshore wind farms. However, aeroacoustic noise is closely related to the aerodynamics around WT blades, and the acoustic detection method requires the mastery of noise emission characteristics. In this paper, FAST.Farm, combined with the acoustic model in OpenFAST, is utilized to investigate the acoustic noise emission characteristics from two 3.4 MW-130 WTs with wake interference. Multi-microphone positions were investigated for the optimal reception selection under 8 m/s and 12 m/s wind speeds with a typical offshore atmospheric turbulence intensity of 6%. The numerical simulation results indicate that wake deficit reduces the total noise emission by about 6 dBA in the overall sound pressure level (OASPL) at 8 m/s, while wake turbulence marginally increases it and its fluctuation. There is a mutual influence between these effects, and the wake deficit effect can be 100% compensated for in the OASPL at 12 m/s. Additionally, downstream observer locations are suggested based on comparisons. These investigations provide new insights into wake interference in offshore wind farms.

Keywords: wind energy; offshore wind turbine; wake interference; aeroacoustic noise model



Citation: Yan, Y.; Xue, L.; Wang, J.; Yang, Z.; Xue, Y. A Numerical Investigation on the Aeroacoustic Noise Emission from Offshore Wind Turbine Wake Interference. *J. Mar. Sci. Eng.* **2024**, *12*, 1988. <https://doi.org/10.3390/jmse12111988>

Academic Editor: Unai Fernández Gámiz

Received: 13 September 2024

Revised: 21 October 2024

Accepted: 31 October 2024

Published: 4 November 2024



Copyright: © 2024 by the authors. Licensee MDPI, Basel, Switzerland. This article is an open access article distributed under the terms and conditions of the Creative Commons Attribution (CC BY) license (<https://creativecommons.org/licenses/by/4.0/>).

1. Introduction

It has been several years since the United Nations proposed the initiative regarding net-zero emissions by 2050 [1]. As one of the most mature renewable energy sources, wind energy plays a crucial role in achieving this ambitious goal [2]. In 2023, a record-high 117 GW of new wind power was installed worldwide, representing a 50% hike from the previous year [3]. Due to rapidly growing ambition, offshore wind took its market share in global new installations from 4% in 2013 to 9% in 2023 [3], significantly contributing to future wind power growth.

It is known that the noise of onshore WTs is a troublesome problem because it has an adverse impact on people's daily lives [4]. This drawback seems negligible since offshore WTs are deployed far from residential areas. However, the noise of offshore WTs also has a potential impact on sea-birds [5] and marine organisms [6,7], which is currently being explored. This paper does not focus on the drawbacks of WT noise but rather on the utilization of it. Wake interference between offshore wind turbines is more severe than that between onshore turbines due to lower turbulence intensity. Therefore, the wake of the previous turbine has a greater impact on the subsequent turbine, such as power loss [8,9] and fatigue load increase [10–12]. To mitigate such issues, some researchers have proposed Active Wake Control (AWC) technology [13,14], which relies on effective wake detection techniques for its implementation, which can improve the timeliness and effectiveness of AWC and reduce fiscal losses. Therefore, this paper mainly explores the noise characteristics of WTs after being affected by a wake, providing data support for exploring an acoustic method for wake detection.

When a fluid flows over the surface of a blade airfoil, a boundary layer is formed near the airfoil surface. Starting from the leading edge, the mainstream flow tube gradually becomes thinner, the flow velocity gradually increases, and the pressure gradually decreases, resulting in a favorable pressure gradient ($\partial p/\partial x < 0$). As the mainstream flows backward to a certain point, the flow tube is the thinnest, while the flow velocity is the fastest, and the pressure is the minimum ($\partial p/\partial x = 0$). Further back, the flow tube becomes thicker, the flow velocity slows down, and the pressure gradually increases again, resulting in an adverse pressure gradient ($\partial p/\partial x > 0$). Early theoretical and experimental studies of turbulent boundary layers (TBLs) subjected to adverse pressure gradients (APGs) were conducted by Rotta [15] and Clauser [16]. A laminar boundary layer at lower Reynolds numbers mostly covers the blade. There is an FPG and an APG on the suction side of the boundary layer, so the boundary layer is prone to separation at the trailing edge [17]. Subsequently, Harun et al. [18] conducted experiments on boundary layers under favorable and adverse pressure gradients. Spectral analysis showed that large-scale motions are amplified in APG-TBLs, especially in the outer region, while this motion is weakened under the action of FPGs. Sajadmanesh et al. [19] studied the vortex dynamics in the boundary layer on the suction side of low-pressure turbine blades under different Reynolds number conditions and found that at high Reynolds numbers, due to Kelvin–Helmholtz instability, a fully turbulent boundary layer is more likely to be formed. Aeroacoustics [20] is the study of flow-induced noise, and this noise is generated by either aerodynamic forces acting on a surface or flow turbulence that may or may not interact with a surface [21]. This interaction between the airfoil surface and the turbulent boundary layer leads to the instability of the boundary layer, generating a pressure fluctuation. This fluctuation is amplified at the airfoil's trailing edge, thus producing noise [22]. When two fluids with different velocities, such as the wake of a WT and incoming turbulence, interact, if there is a velocity difference and shear force, it may trigger more severe Kelvin–Helmholtz instability, thereby changing the characteristics of the turbulent boundary layer around the blade and affecting the acoustic characteristics of WT blades.

WT wakes mainly exhibit two main characteristics: wake-induced velocity deficit and wake turbulence generated due to the instability of the shear layer caused by the rupture of the tip vortex when the wake transitions from the near-wake region to the far-wake region [23]. Wake deficit reduces downstream wind speed, while wake turbulence increases the atmospheric turbulence intensity. Offshore wind farm wakes can affect the angle of attack of the blade, thereby influencing the boundary layer characteristics of the blade airfoil, including boundary layer thickness, turbulence content, etc., thus affecting their self-noise characteristics. Therefore, they will have an intrinsic relationship, allowing for the acoustic detection method of offshore wind farm wakes.

Aerodynamic noise mainly originates from the trailing edge of WT blades, which demonstrates the characteristics of amplitude modulation noise (AMN) [24]. A schematic of WT aerodynamic noise is shown in Figure 1, which is mainly divided into turbulent inflow (TI) noise [25] and airfoil self-noise [26]. Pressure oscillations produce TI noise following the unsteady loading generated on the blades due to the incoming wind turbulence. Self-noise is generated from the interaction of an airfoil with its boundary layer and near wake.

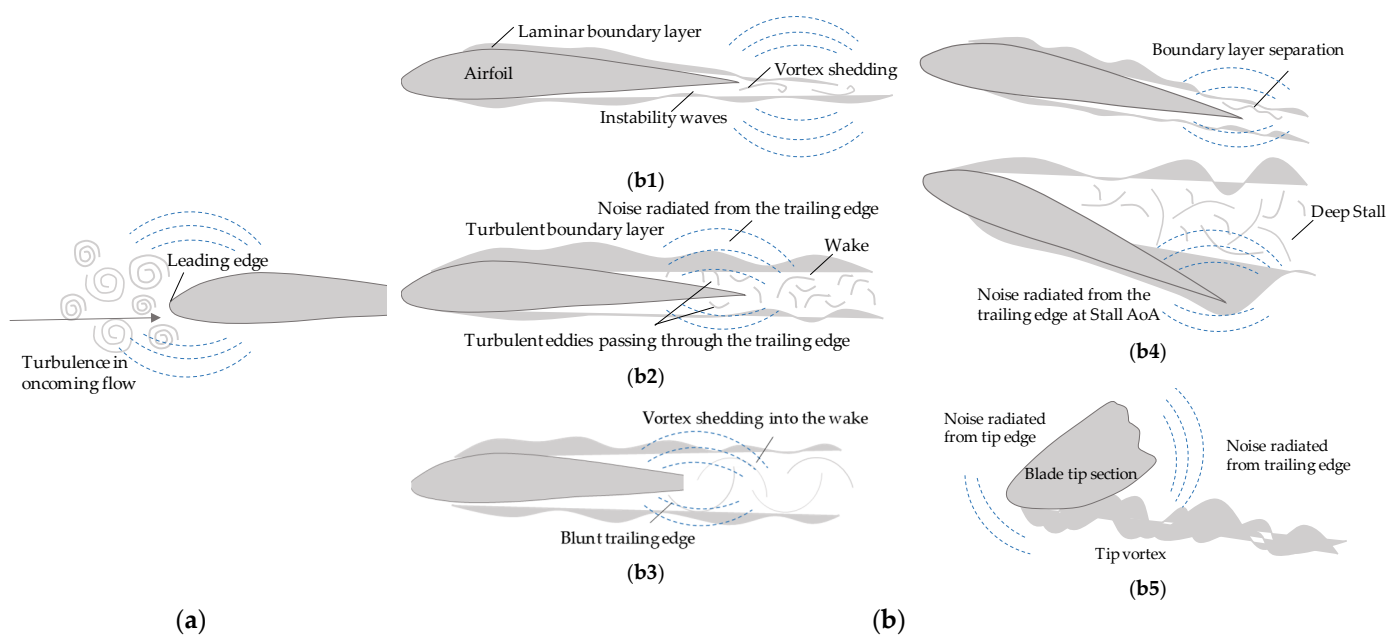


Figure 1. Schematic of WT aerodynamic noise sources. (a) TI noise. (b) Airfoil self-noise: (b1) laminar boundary layer–vortex shedding noise, (b2) turbulent boundary layer–trailing edge (TBL-TE) noise, (b3) trailing edge bluntness noise, (b4) separation–stall noise, and (b5) tip vortex noise [27,28].

Currently, Computational Fluid Dynamics (CFD) and Ffowcs Williams–Hawkins (FW-H) for far-field noise calculations are widely used in aerodynamic noise calculation [29,30], but their high accuracy is accompanied by an extremely higher level of consumption of computational resources. In this case, the model based on simplified mathematical formulas stands out [31], because this kind of computation method is faster and consumes fewer computational resources.

For airfoil self-noise, this group of noise sources was first modeled in 1989 by Brooks, Pope, and Marcolini [28], who distinguished five noise mechanisms among turbulent boundary layer–trailing edge (TBL-TE), laminar boundary layer–vortex shedding, trailing edge bluntness, separation–stall, and tip vortex noise, as shown in Figure 1b. Originally, they conducted many experiments on NACA0012 airfoils of different chords, considering different inflow wind speeds and angles of attack. Such activity led to the definition of a semi-empirical model, commonly named BPM, and formulas. Subsequently, Parchen [32] of TNO, a Dutch institution, developed a more physical TBL-TE noise model for the TBL-TE noise source, known as the “TNO” model, which combined surface pressure fluctuation calculations with the theory of far-field acoustic spectral prediction. Although the TNO model is a newer model for calculating TBL-TE noise sources, the BPM model is still widely used in estimating self-noise after modification for its simplicity. Therefore, this paper uniformly chose the BPM model to estimate blade self-noise.

Another major noise source is TI noise. Amiet [27], Paterson, and Amiet [33] modeled a flat plate placed in turbulence, developed the Amiet noise model, and gave a calculation formula for calculating TI noise. This was the first characterization of the TI noise source. Since then, researchers have made many attempts to estimate this noise source, but the results are still unsatisfactory. Guidati et al. [34] corrected the sound pressure level (SPL) by adding a term that considers the airfoil profile shape and camber angle, but it turned out that this method was too computationally expensive for WT simulation. To reduce the computational cost, a simplified Guidati model was subsequently proposed by Moriarty et al. [35], but it was confirmed that its simulation results deviated greatly from the actual results. This paper uses a model that combines the modified Amiet and simplified Guidati to estimate turbulent inflow noise to maximize the accuracy of calculation.

The noise model used in this paper is shown in Table 1:

Table 1. Selection of aerodynamic noise calculation model.

Aerodynamic Noise Type	Computational Model
Airfoil self-noise TI noise	BPM Amiet + Simplified Guidati

As for the wake model, considering the computational cost and accuracy requirements, the Dynamic Meandering Wake (DWM) model based on the simplified CFD method is selected [36,37]. In addition, the impact of wind farm clusters is not considered in this paper, so the DWM model, the accuracy of which has already been proven, especially in predicting the wake characteristics of a single WT, is selected here [38].

According to the authors' review of the existing literature, research on the correlation between wake interference and the aerodynamic noise of WTs is rare. However, the existing literature on flow ingestion by the rotating blades of propellers is extensive, and there are some correlations between them. Petricelli et al. [39] experimentally studied the influence of inflow on the aerodynamic acoustics of unmanned aerial vehicle propellers and found that for broadband noise, airfoil self-noise was the main contribution. Celik et al. [40] experimentally conducted a comprehensive study on the noise radiation characteristics of two rotors immersed in turbulence in a tandem configuration and found that in the low- and medium-frequency bands, the SPL of airfoil self-noise increases and shows obvious intermittency and amplitude modulation characteristics. Zaman et al. [41] experimentally studied the aerodynamic and acoustic characteristics of propellers under the action of turbulent boundary layers in different planes and found that the increase in tonal noise and broadband noise is mainly attributed to the increase in the turbulent content of the boundary layer itself.

As for research on the influence of wake interference on the aerodynamic noise of WTs, the earliest study was in 2010: Heimann et al. [42] found that the wake flow favors the sound propagation from the upper sources towards the ground by using numerical simulations. Then, DTU (Technical University of Denmark) conducted further research. Barlas et al. [43] performed unsteady acoustic simulations using AL/LES (Actuator Line/Large Eddy Simulation) input and adopted a dynamic source approach to simulate rotating turbine blades and found that the effect of wakes on far-field noise prediction is non-negligible, especially under stable atmospheric conditions. Through experiments and numerical simulations on HAWC2, Bertagnolio et al. [44] confirmed the fact that wake turbulence did truly increase the aerodynamic noise emissions of downstream WTs and found that the noise emission of WTs is closely related to their rotor speed.

The above studies all focus on the impact of noise emission from WTs on the environment. Based on considering multi-observer positions, this paper attempts to explore the feasibility of the acoustic detection of wake interference through analysis, and the work in this paper is mainly divided into the following four points:

- (1) The AM noise characteristics of the A-weighted overall sound pressure level (OASPL) signal were explored to verify the correctness of this numerical simulation method.
- (2) Under the condition of steady wind inflow, the influence of wake interference on the aerodynamic noise of a WT was preliminarily compared and analyzed. Both 8 m/s and 12 m/s were considered as two wind speed conditions.
- (3) Under the condition of turbulent wind inflow, the influence of wind speed on the aerodynamic noise of a single WT was investigated, as well as the sensitivity of the noise signal to turbulence.
- (4) Based on one study (3), two wind speeds, 8 m/s and 12 m/s, were selected, and the difference in and optimal performance of aerodynamic noise when the WT was or was not suffering from wake interference were further verified and analyzed in combination with the WT's output parameters. The most sensitive observer position was also explored under multiple microphone settings.

The structure of this paper is laid out as follows: The software, model, WT reference coordinate system, wind conditions, and simulation settings are introduced in Section 2. In Section 3, the effect of wake interference on WT aerodynamic noise emission under different wind conditions and observer positions was investigated through comparative analysis. Finally, Section 4 presents the conclusions of this study on how wake interference affects WT aerodynamic noise emission, as well as the shortcomings and future research directions.

2. Methods and Materials

2.1. Dynamic Analysis Tool

FAST.Farm is a medium-fidelity multi-physical engineering tool based on some of the principles of the DWM model but addresses many of the limitations of DWM implementation [45]. In FAST.Farm, OpenFAST is used to solve the aero-hydraulic-servo-elastic dynamics problem for each WT, while the additional physical properties of the wind farm ambient wind and the wake characteristics are taken into consideration, and the wind farm super controller is provided.

The main idea behind the DWM model is to capture the wake characteristics associated with accurately predicting wind farm power performance and WT loads, including velocity deficit, wake meandering, and wake-added turbulence, but with appropriate simplification to minimize computational expenses.

The entire simulation process is shown in Figure 2.

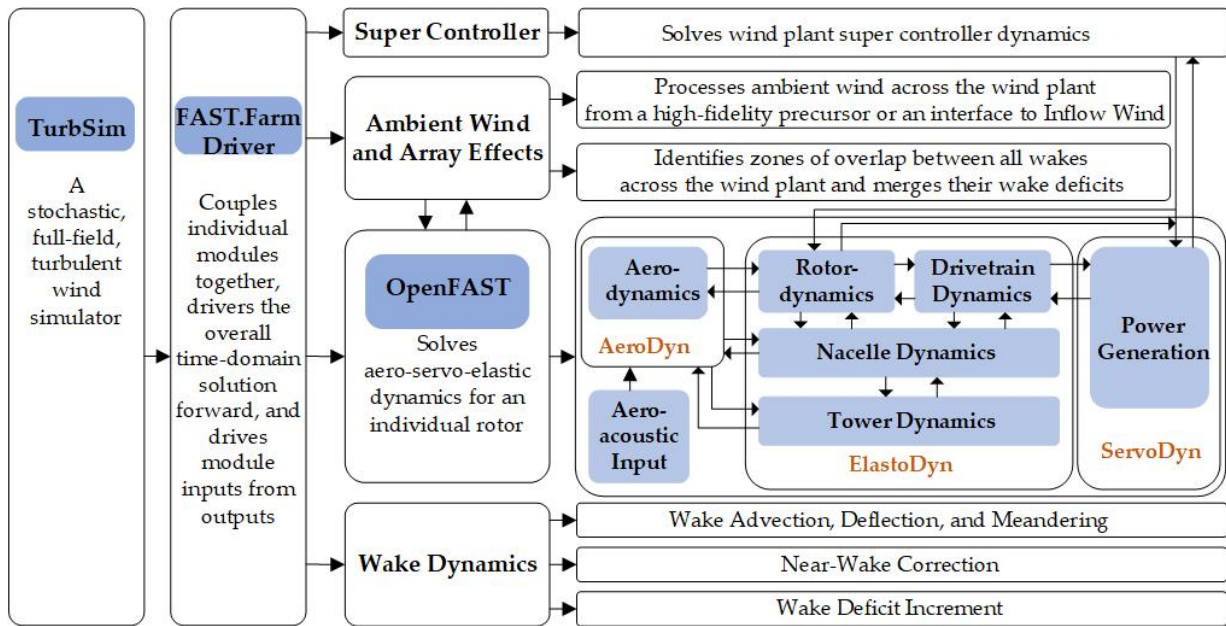


Figure 2. A schematic diagram of the entire simulation process [45,46].

2.2. Turbine Characteristics

In this study, all the turbines used in the simulation were the 3.4 MW reference WT in IEA Wind Task 37 [47]. It has a power rating of 3.37 MW, a rotor diameter of 130 m, and a hub height of 110 m. The cut-in and cut-out wind speeds are 4 m/s and 25 m/s, respectively. A more detailed introduction of the WT model’s parameters is shown in Table 2:

Table 2. The main parameters of the WT model [47].

Parameters	Value	Parameters	Value
Rotor diameter	130 m	Nacelle tilt angle	5°
Hub height	110 m	Rated rotor speed	11.75 rpm
Cut-in wind speed	4 m/s	Rated tip-speed ratio	8.16 m/s
Cut-out wind speed	25 m/s	Max tip-speed ratio	80 m/s
Rated electrical power	3.37 MW	Maximum aerodynamic Cp	0.418

2.3. Aeroacoustic Noise Calculation

To deploy efficient and quiet WTs at low-wind-speed sites, the National Renewable Energy Laboratory (NREL) made a comprehensive research effort to improve the understanding of WT aerodynamic acoustics. The aerodynamic acoustics model is coupled with OpenFAST to estimate the aerodynamic noise of a single WT, which is used to predict the aerodynamic noise emission and the SPL information at the observation point. Based on the implementation of NAFNoise, a semi-empirical code is developed, and its verification is provided in [35]. In this paper, the Amiet model and simplified Guidati model are used to calculate the turbulent inflow noise, and the BPM model is used to calculate the noise from other noise sources; more details about this calculation method can be found in [48].

2.3.1. Amiet and Simplified Guidati Model

When an object is immersed in turbulence, surface pressure fluctuations will be generated, and noise will be radiated; this noise is called the turbulent inflow noise. In OpenFAST, the formula defined by Moriarty et al. [49] is adopted. This formula is based on the work of Amiet [27,33] and considers the airfoil thickness.

The model starts by first computing the wave number:

$$k_1 = \frac{2\pi f}{U_1} \tag{1}$$

where U_1 is the incident inflow velocity on the profile. From k_1 , the wave numbers $\overline{k_1}$ and \hat{k}_1 are computed:

$$\overline{k_1} = \frac{k_1 c_i}{2} \tag{2}$$

$$\hat{k}_1 = \frac{k_1}{k_e} \tag{3}$$

where c_i is the local chord, and k_e is the wave number range of energy-containing eddies, defined as follows:

$$k_e = \frac{3}{4L_t} \tag{4}$$

L_t is the turbulent length scale, as the default implementation, and L_t is defined following the formulation proposed in Zhu et al. [50]:

$$L_t = 25z^{0.35}z_0^{-0.063} \tag{5}$$

where z is the height above the ground of the leading edge of section i at a given instant, while z_0 is the surface roughness.

The value of the SPL is expressed in one-third octave bands at the given frequency, f , originating at the given blade station, i , which can be computed as follows:

$$SPL_{TI} = 10\lg \left(\rho^2 c^4 \frac{L_t d}{2r_e^2} M^5 I_1^2 \frac{\hat{k}_1^3}{(1 + \hat{k}_1^2)^{\frac{7}{3}}} \overline{D} \right) + 78.4 \tag{6}$$

where ρ is the air density, c the speed of sound, d the blade element span, r_e the effective distance between the leading edge and observer, M the Mach number, I_1 the turbulence intensity of the airfoil inflow, and \bar{D} the directivity term. \bar{D} is different below (\bar{D}_l) and above (\bar{D}_h) a certain frequency, which is named the “cut-off” and defined as follows:

$$f_{co} = \frac{10U_1}{\pi c_i} \tag{7}$$

Two corrections to this model are also implemented. The first one comprises a correction for the angle of attack, α . This correction is formulated as follows:

$$SPL_{TI} = SPL_{TI} + 10\lg(1 + 9a^2) \tag{8}$$

The second correction is called low-frequency correction (LFC) and is formulated as follows:

$$S^2 = \left(\frac{2\pi\bar{k}_1}{\beta^2} + \left(1 + 2.4\frac{\bar{k}_1}{\beta^2} \right)^{-1} \right)^{-1} \tag{9}$$

$$LCF = 10S^2 M\bar{k}_1^2 \beta^{-2} \tag{10}$$

$$SPL_{TI} = SPL_{TI} + 10\lg\left(\frac{LFC}{1 + LFC}\right) \tag{11}$$

S^2 represents the squared Sears function, and β^2 is the Prandtl–Glauert correction factor, which is defined as follows:

$$\beta^2 = 1 - M^2 \tag{12}$$

Since the modified Amiet model often overpredicts the sound spectrum, Moriarty et al. [51] proposed a simplified model based on the geometric characteristics of six wind turbine airfoils. The validity of the correction is limited to Mach numbers on the order of $0.1 \approx 0.2$ and Strouhal number S_t below 75. S_t is defined based on the airfoil chord and mean inflow velocity:

$$S_t = \frac{f c_i}{U_1} \tag{13}$$

The modified formula is as follows:

$$t = t_{1\%} + t_{10\%} \tag{14}$$

$$\Delta SPL_{TI} = -(1.123t + 5.317t^2)(2\pi S_t + 5) \tag{15}$$

where $t_{x\%}$ is the relative thickness of the profile at the x position along the chord (0% being the leading edge and 100% the trailing edge).

2.3.2. BPM Model

Turbulent Boundary Layer–Trailing Edge Noise

An airfoil immersed in a flow will form a boundary layer. At high Reynolds numbers, the boundary layer is turbulent. When the turbulence passes through the trailing edge, noise will be generated. This noise is the *TBL–TE* noise and is the aerodynamic acoustic noise source of the modern WT rotor.

The *SPL* of the *TBL–TE* noise in the BPM model is made from three contributions:

$$SPL_{TBL-TE} = 10\lg\left(10^{\frac{SPL_p}{10}} + 10^{\frac{SPL_s}{10}} + 10^{\frac{SPL_\alpha}{10}}\right) \tag{16}$$

where the subscripts p , s , and α refer to the contributions of the pressure side, suction side, and angle of attack, respectively.

For the suction and pressure contributions, the equations are as follows:

$$SPL_p = 10lg \left(\frac{\delta_p^* M^5 d \overline{D}_h}{r_e^2} \right) + A \left(\frac{St_p}{St_1} \right) + (K_1 - 3) + \Delta K_1 \quad (17)$$

$$SPL_s = 10lg \left(\frac{\delta_s^* M^5 d \overline{D}_h}{r_e^2} \right) + A \left(\frac{St_s}{St_1} \right) + (K_1 - 3) \quad (18)$$

where δ^* is the boundary layer thickness on both sides of the airfoil, S_t is the Strouhal number based on δ^* , $A, A', B, \Delta K_1, K_1, K_2$ are empirical functions based on S_t , and \overline{D}_h is the high-frequency directivity index.

For the angle of attack contribution, a distinction is made above and below the stall angle, which in the original BPM model is set equal to 12.5 degrees, whereas it is here assumed to be the actual stall angle of attack of the airfoil at blade station i . Below the stall point, SPL_α is equal to the following:

$$SPL_\alpha = 10lg \left(\frac{\delta_s^* M^5 d \overline{D}_h}{r_e^2} \right) + B \left(\frac{St_s}{St_2} \right) + K_2 \quad (19)$$

At angles of attack above the stall point, the airflow along the airfoil profile is completely separated, and noise is radiated from the entire airfoil chord. At this time, the contributions of the pressure and suction sides are set to $-\infty$. At this time, the angle of attack contribution is as follows:

$$SPL_\alpha = 10lg \left(\frac{\delta_s^* M^5 d \overline{D}_l}{r_e^2} \right) + A' \left(\frac{St_s}{St_2} \right) + K_2 \quad (20)$$

Notably, above the stall point, the low-frequency directivity \overline{D}_l is adopted.

Tip Vortex Noise

The interaction between the vortex and the blade tip or the trailing edge near the tip generates tip vortex noise. The SPL estimate of this noise source is as follows:

$$SPL_{Tip} = 10lg \left(\frac{M^2 M_{max}^2 l^2 \overline{D}_h}{r_e^2} \right) - 30.5(lg St'' + 0.3)^2 + 126 \quad (21)$$

$M_{max} = M_{max}(\alpha_{tip})$ is the maximum Mach number, measured near the blade tip position in the separated flow region and depends on the angle of attack α_{tip} at the tip blade. l is the spanwise range of the separated flow, and St''' is the Strouhal number based on l .

For the round shape of the tip, l is estimated as follows:

$$l = c_i 0.008 \alpha_{tip} \quad (22)$$

For a square tip, the BPM model estimates l based on the quantity, α'_{tip} , which is defined as follows:

$$\alpha'_{tip} = \left[\left(\frac{\partial L'}{\partial y} \right)_{y \rightarrow tip} \right] \alpha_{tip} \quad (23)$$

where L' is the lift per unit span along the blade at position y .

For α'_{tip} between 0 and 2 degrees, l becomes the following:

$$l = c_i (0.0230 + 0.0169 \alpha'_{tip}) \quad (24)$$

while for α'_{tip} larger than 2 degrees, l is

$$l = c_i(0.0378 + 0.0095\alpha'_{tip}) \tag{25}$$

Trailing Edge Bluntness Noise

Trailing edge bluntness noise is generated due to the existence of a certain thickness at the trailing edge of WT blades. The frequency and amplitude of this noise source depend on the geometry of the trailing edge and have typical tonal characteristics. It is defined as follows:

$$SPL_{TEB-VS} = 10\lg\left(\frac{\delta_p^* M^5 d \bar{D}_h}{r_e^2}\right) + G_4\left(\frac{h}{\delta_{avg}^*}, \Psi\right) + G_5\left(\frac{h}{\delta_{avg}^*}, \Psi, \frac{St''}{St''_{peak}}\right) \tag{26}$$

In the equation, δ_{avg}^* is the average displacement thickness for both sides of the airfoil. Note that this noise source is very sensitive to h and Ψ .

2.3.3. A-Weighting

All analysis data are A-weighted in this paper, which is the experimental coefficient that aims to consider the sensitivity of human hearing to different frequencies. In this case, this study is more biased towards airfoil self-noise. The A-weight, A_w , is computed as follows:

$$A_w = \left[10\lg\left(1.652339 \frac{f^4}{(f^4+107.65265^2)(f^2+737.86223^2)}\right) + 10\lg\left(2.422881e16 \frac{f^4}{(f^2+20.5989972)^2(f^2+12194.222)^2}\right) \right] / \lg 10 \tag{27}$$

The A-weighting is a function of frequency and is added to the values of the SPL:

$$SPL(f_i)_{A_w} = SPL(f_i) + A_w \tag{28}$$

2.4. WT Reference Coordinate System and Direction Setting

Before performing the simulation, the position must be specified within the OpenFAST global inertial coordinate system, which is located at the base of the tower, with the x-axis pointing downwind, the y-axis pointing in the transverse direction, and the z-axis pointing vertically upward. The WT reference coordinate system is shown in Figure 3:

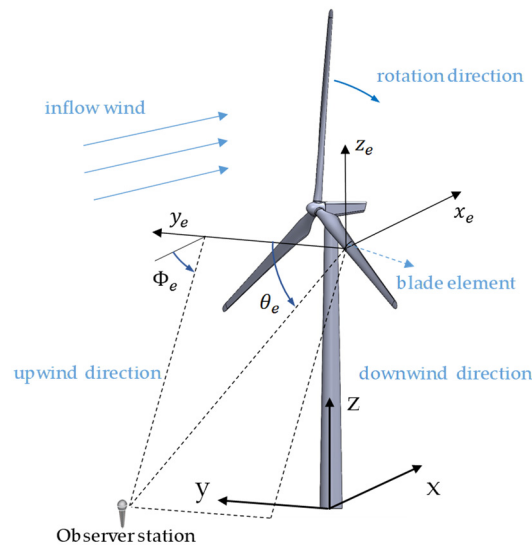


Figure 3. The WT reference coordinate system and directivity angles.

The directivity of the BPM model is used, and the directivity term \bar{D} corrects the SPL according to the relative distance between the observer and the noise source. The span direction angle describes the position of the observer Φ_e and chord direction angle θ_e , which are schematically represented in Figure 3 and defined as follows:

$$\Phi_e = \text{atan}\left(\frac{z_e}{y_e}\right) \tag{29}$$

$$\theta_e = \text{atan}\left(\frac{y_e \cdot \cos(\Phi_e) + z_e \cdot \sin(\Phi_e)}{x_e}\right) \tag{30}$$

2.5. Ambient Wind Conditions

TurbSim [52], a stochastic, full-field, turbulent wind simulator, was mainly used to generate two turbulent winds, including two typical different average wind speeds and one turbulence intensity. These outputs will be transmitted to FAST.Farm as input information. The ambient wind conditions are shown in Table 3.

Table 3. Wind conditions and wave condition setting.

Parameter	Value	
Mean wind speed	8 m/s	12 m/s
TI	0.06	
Turbulence model	IECKAI	
Shear power law exponent	0.20	

The IEC Kaimal (IECKAI) model was also selected as our wind spectral model. The IECKAI model assumes neutral atmospheric stability, which is defined in IEC 61400-1 3rd ed. [53].

The spectra for the three wind components ($K = u, v, w$) are given by

$$S_K(f) = \frac{4\sigma^2 L_K / u}{(1 + 6f \cdot L_K / u)^{5/3}} \tag{31}$$

where f is the cyclic frequency, u is the mean wind speed at hub height, σ is the standard deviation and can be estimated by the turbulent inflow, and L_K is an integral scale parameter.

σ is defined as follows:

$$\sigma = TI \cdot u \tag{32}$$

The integral scale parameter is defined as follows according to IEC 61400-1 3rd ed. [53].

$$L_K = \begin{cases} 8.10 \cdot 0.7 \cdot 60, & K = u \\ 2.70 \cdot 0.7 \cdot 60, & K = v \\ 0.66 \cdot 0.7 \cdot 60, & K = w \end{cases} \tag{33}$$

2.6. Simulation Settings

FAST.Farm integrates the entire simulation experiment. The simulation is conducted within a large flow field, and to minimize external influences, all the time, the simulations proposed in this paper use the same flow field.

According to the grid setting standard in FAST.Farm [45] and TurbSim [52], the low-resolution region is set as $X \times Y \times Z = 2120 \times 800 \times 290$ m, the high-resolution region is $X \times Y \times Z = 160 \times 160 \times 200$ m, and two high-resolution regions are set according to the simulation conditions, and the grid size for each cell is set to 10 m, as shown in Figure 4. To ensure accuracy, the time steps of the FAST output and OASPL output are both set to 0.00625 s, and the turbulent wind generation time step is set to 0.1 s. It is worth noting that this simulation also includes a WT controller, which adjusts the rotor speed or blade pitch

angle of the WT to optimize the power output, making it more representative of actual WT operation.

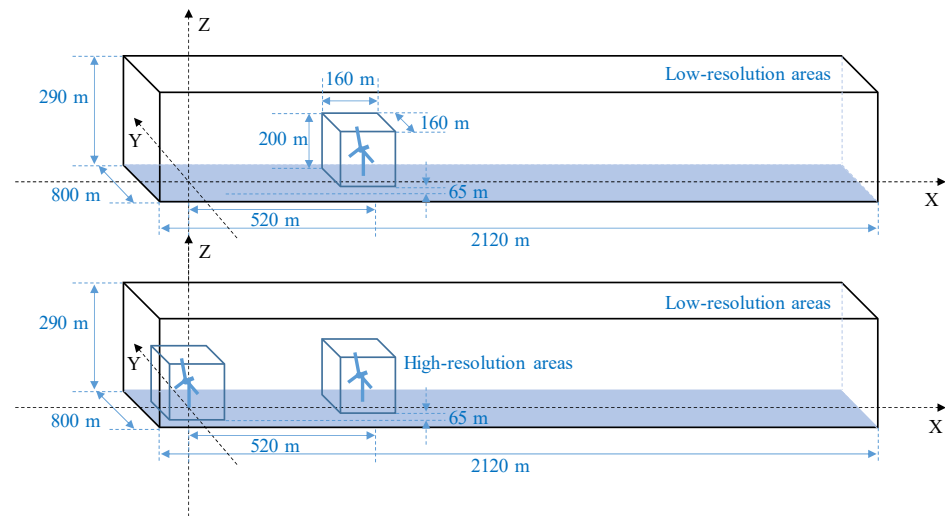


Figure 4. A schematic diagram of the simulation area and the location of the WTs.

The simplest situation in which one WT is affected by the wake of another WT was considered in this paper. Various operating conditions were analyzed, and the differences in aeroacoustic noise between a WT with wake interference and one without wake interference were explored using a combination of time-domain and frequency-domain methods.

3. Simulation Results

Firstly, the details about observer location settings are described. Secondly, the amplitude modulation (AM) characteristics of the simulation results are verified. Finally, the time-frequency analysis method is used to further explore the relationship between wake interference and the aeroacoustic noise emission of the WT under different conditions.

3.1. Observer Location Setting

Due to the directionality of WT noise, multi-microphone positions were set to explore the most sensitive observer position to WT wake interference. Twelve different positions were selected, and the specific position coordinates are shown in Table 4.

Table 4. Observer position setting.

Name	Location Coordinates	Name	Location Coordinates
Observer 1	(−124, −124, 0)	Observer 7	(−124, 124, 0)
Observer 2	(0, −175, 0)	Observer 8	(−175, 0, 0)
Observer 3	(124, −124, 0)	Observer 9	(175, 0, 90)
Observer 4	(175, 0, 0)	Observer 10	(175, 0, 110)
Observer 5	(124, 124, 0)	Observer 11	(0, 0, 110)
Observer 6	(0, 175, 0)	Observer 12	(0, 0, 0)

Observers 1–10 are placed according to the IEC 61400-11 standard [54], where the distance from the WT is the hub height H of the WT plus half of the diameter of the WT impeller D , that is $H + D/2$. Observers 1–8 are placed based on the positions of directional exploration, and the specific location is a circle around the WT on the ground, with an angle interval of 45° . Observers 9 and 10 are positioned to accommodate microphone placements at different heights above the ground in the downwind direction. Finally, considering the operability of the installation in the actual offshore situation, the microphone positions above the hub and at the base of the tower are considered, which correspond to Observer 11 and Observer 12, respectively. A more distinct diagram is shown in Figure 5.

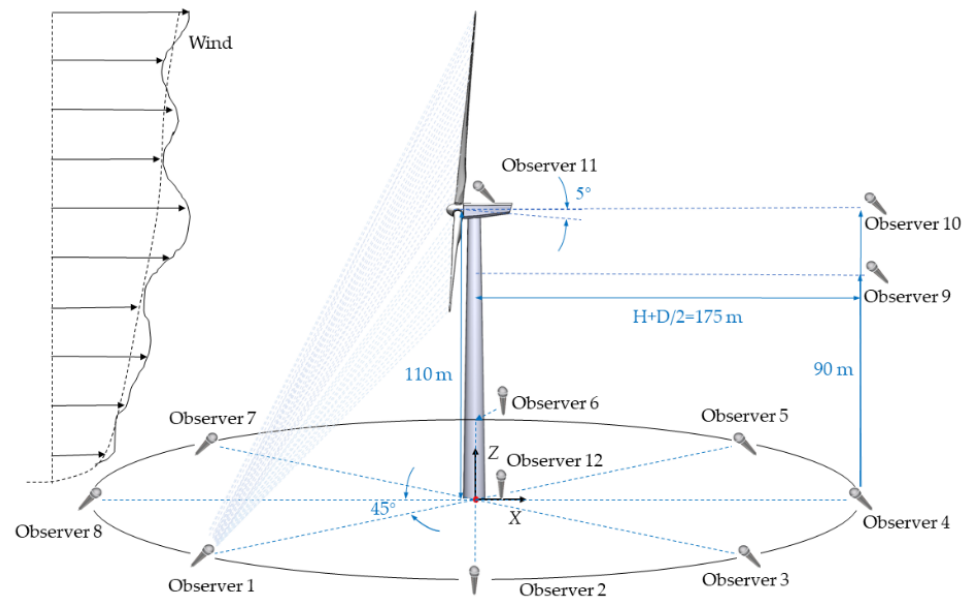


Figure 5. Schematic diagram of observer position setting.

3.2. AM Noise Verification and Analysis

Amplitude modulation noise (AMN) (or Swish-Swish sound) is recognized as the airfoil self-noise with rotation motion [24]. This noise has a pronounced Doppler effect and exhibits a strong correlation with the blade passing frequency (BPF), which is also considered a BPF noise.

To verify whether the simulation results have obvious AMN characteristics, we selected the steady wind condition of 8 m/s in Zone II for the initial exploration and intercepted the time-domain OASPL data of the 70th lap for analysis, when the speed of the WT is 9.26 rpm, and its one-revolution time is about 6.50 s. Observer 1 is selected here.

In Figure 6a, three peaks are obviously observed, representing the successive sweeping of three blades. To explore its spectral characteristics, the FFT was performed on the time-domain OASPL signals. The result is shown in Figure 6b. According to the spectrum analysis results, the frequency peak occurs at 0.46 Hz. The BPF calculation formula is as follows:

$$BPF = \frac{rpm \times n}{60} \quad (34)$$

where *rpm* is the speed of the WT at this time, and *n* is the number of WT blades.

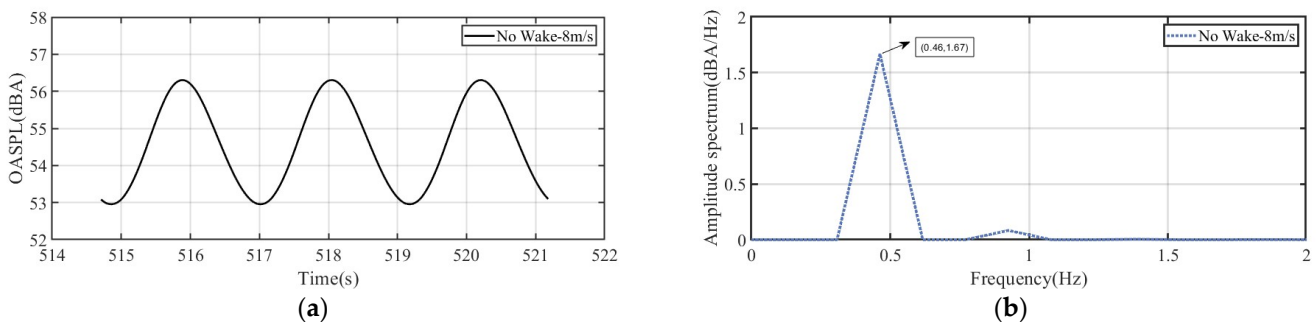


Figure 6. One revolution of the WT: (a) overall sound pressure level (OASPL); (b) corresponding amplitude spectrum.

Within an acceptable error range, the calculated BPF value is exactly the corresponding peak frequency on the spectrum results, which verifies the hypothesis. Accordingly, the

numerical simulation results show the AMN characteristics well, further validating the correctness of simulation outcomes.

3.3. Steady Wind Conditions

To preliminarily explore the influence, steady wind conditions at two wind speeds, 8 m/s (below the rated wind speed) and 12 m/s (above the rated wind speed), were explored here. The analysis combines the outputs of the WT and covers both the time and frequency domains. The calculation results from Observer 1 are selected for analysis across all steady conditions.

3.3.1. Below Rated Wind Speed of 8 m/s

In the first 100 s of the simulation, the upstream WT started, and its wake began to develop, with the downstream WT not yet affected by wake interference, so the OASPL signals of both turbines nearly coincided. After 100 s, the wake of the front WT reached the rear, and the OASPL signals of the rear WT were significantly reduced, which proves that the wake truly affects the aeroacoustic noise emission of the downstream WT. This phenomenon is also visually confirmed in Figure 7. Moreover, the velocity deficit is more pronounced below the rated wind speed, resulting in lower noise levels radiated by the downstream WT.

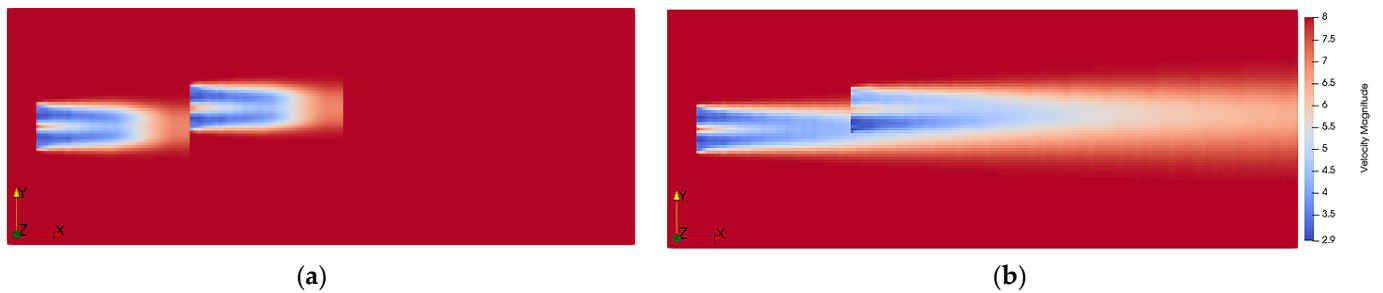


Figure 7. Visualization of wake under 8 m/s steady wind condition: (a) wake development; (b) fully developed wake.

According to the results shown in Figure 8, to avoid the influence of the first time periods of the simulation on the analysis results, data in the interval of 400 s–1000 s were selected for subsequent analysis, with a total duration of 600 s.

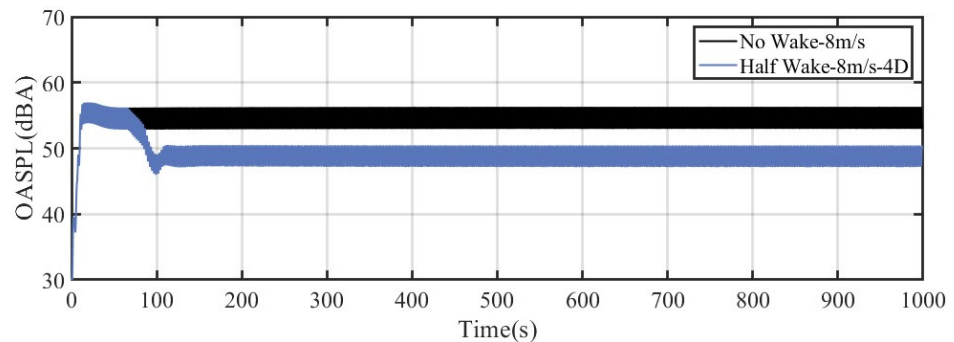


Figure 8. The OASPL of the WT in the time domain with and without wake interference during the full simulation period.

Figure 9a shows the amplitude spectrum of the time-domain OASPL. Regardless of whether the WT is affected by the wake, the peaks occur at BPF. It can be observed that in the presence of wake interference, its peak frequency shifts forward. The reason is that the wake deficit effect leads to insufficient downstream wind speed, directly leading to

a decrease to the downstream WT rotor speed. This is also confirmed by the results in Figure 9b,c.

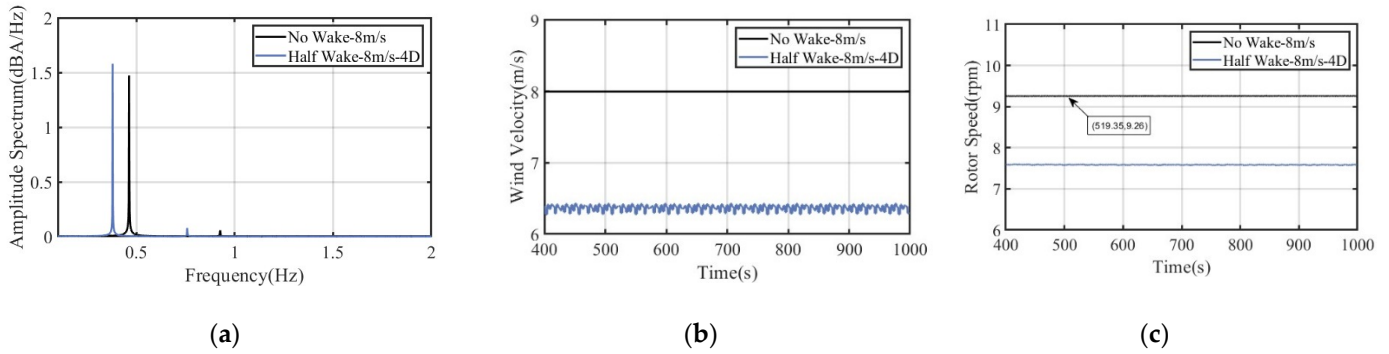


Figure 9. Schematic diagram of comparison of WT with and without wake interference at 8 m/s wind speed: (a) aeroacoustic noise amplitude spectrum, (b) wind speed, (c) rotor speed.

Figure 9b clearly shows that the wind speed of the WT affected by the wake fluctuates, which indicates that the wake of the upstream WT contains a certain amount of turbulence. This effect leads to an increase in the peak at BPF according to Figure 9b.

The effect of wake turbulence is not obvious in Figure 8. Therefore, to make the fluctuations in the OASPL signals more apparent, the peaks and valleys of the time-domain OASPL over a 600 s period were extracted, and then the subsequent valleys were subtracted from the peaks in sequence to obtain the difference between them.

Figure 10 shows the extraction results. It is noted that the filter width of the peak's extraction algorithm is appropriately adjusted to avoid the influence of local extreme values. To clarify the results, Figure 10 only shows the extraction results for 200 s.

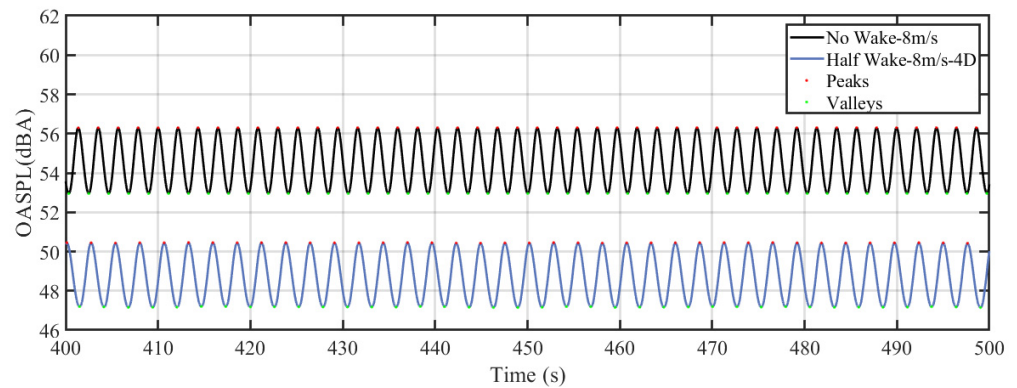


Figure 10. A schematic diagram of the peak and valley extraction results of the 8m/s wind speed in the time domain.

In Figure 11, the difference values of the OASPL signals of the WT without wake interference almost make a straight line, while the other fluctuates obviously. Combined with the comparison results of the wind speed in Figure 9b, it is further confirmed that the wake turbulence truly causes this fluctuation.

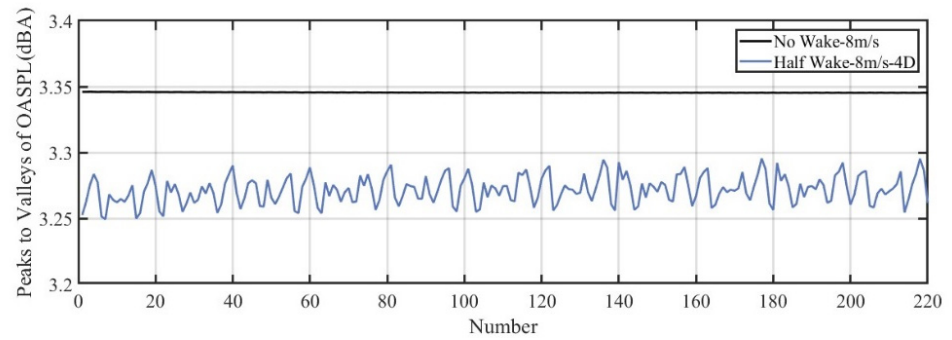


Figure 11. Comparison of peaks to valleys of OASPL with and without wake interference under 8m/s steady wind conditions.

3.3.2. Above Rated Wind Speed of 12 m/s

When the wind speed is increased above the rated wind speed, the absolute values of the OASPL signals in the time domain are almost the same. Therefore, the velocity deficit caused by the wake of the upstream WT can be completely compensated for by increasing the incoming wind speed, and the visualization in Figure 12 can also prove this conclusion.

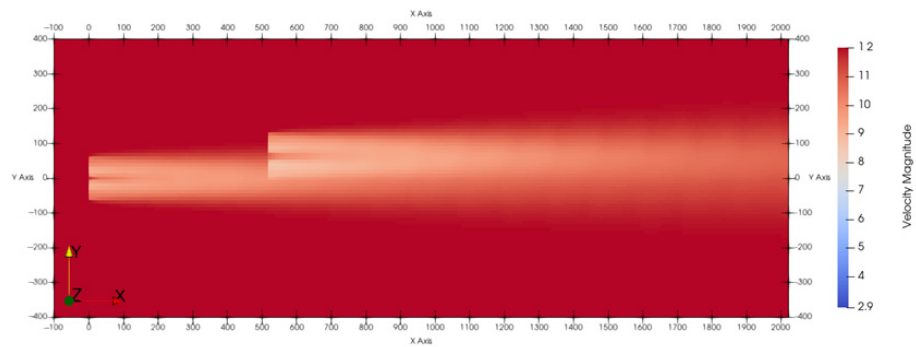


Figure 12. Visualization of wake under 12 m/s steady wind condition.

In Figure 13, when the wind speed is higher than the rated wind speed, the absolute value of OASPL only has a little difference between two conditions. However, the WTs with and without wake interference both reach the rated wind speed, and the rotor speed is almost the same, as shown in Figure 14a,b. In Figure 14b, it is worth noting that the rotor speed of the affected WT has more obvious peak fluctuations, which verifies the existence of wake turbulence. In Figure 14c, it can be seen from the amplitude spectrum diagram that the peak frequencies are almost coincident, which is consistent with the verification result. It should be noted that the frequency peak without wake interference is higher than that with wake interference.

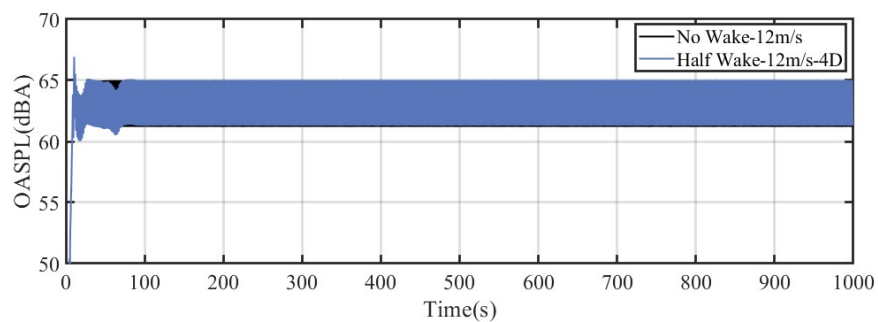


Figure 13. The OASPL of the WT in the time domain with and without wake interference under 12 m/s steady wind conditions.

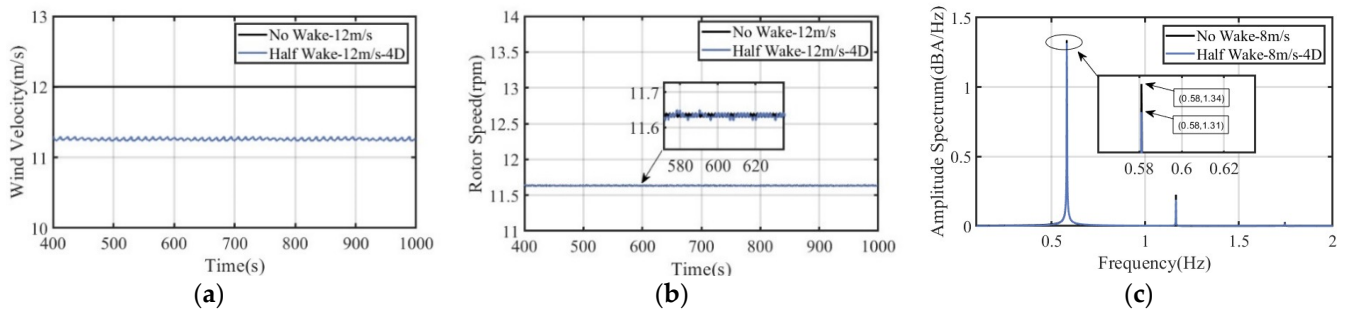


Figure 14. Schematic diagram of comparison of WT with and without wake interference at 12 m/s wind speed: (a) wind speed, (b) aeroacoustic noise amplitude spectrum.

To explore the reason behind the difference about the frequency peak value, further analysis about the one-third octave SPL characteristics of the noise source is done in this paper, as shown in Figure 15. Under wake interference, the OASPL of the TBL-TE noise on the pressure side of the turbulent boundary layer increases slightly in the higher frequency range. The separation–stall noise increases significantly in the middle–frequency range, which indicates that the wake makes the level of vortex shedding on the pressure side of the blade even larger. The wake turbulence increases the angle of attack, which makes the blade more likely to experience the separated stall environment. However, the TBL-TE noise levels on the suction side and the tip vortex noise levels are higher when the WT is not affected by the wake, which indicates that the wake makes the vortex shedding level on the suction side and the tip of the blade lower. Furthermore, the tip vortex noise of the WT with wake interference is reduced more greatly, which is also the reason for the higher frequency peaks in the spectrum for the unaffected WT.

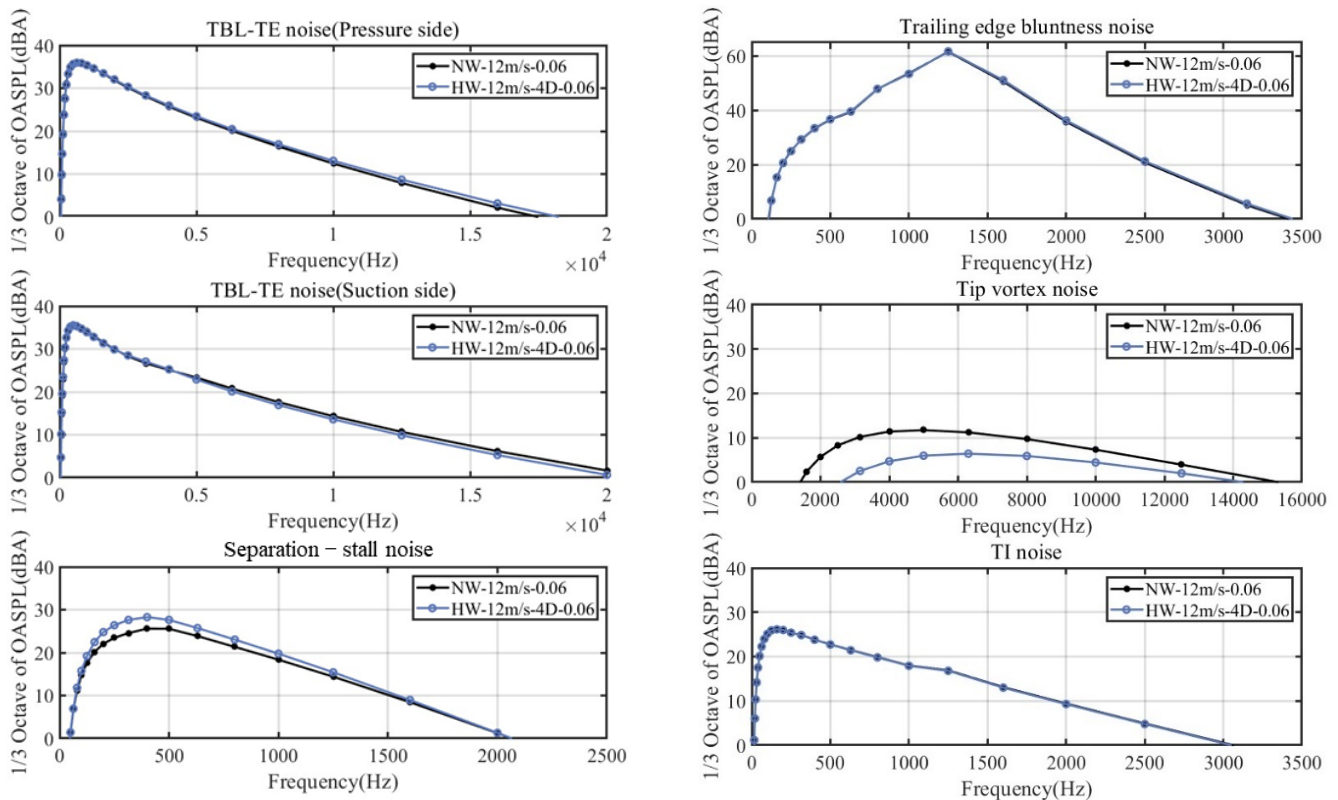


Figure 15. Schematic diagram for comparison of different noise sources of WT noise radiation with and without wake effects at 12 m/s steady wind speed.

Moreover, it is a remarkable fact that the trailing edge bluntness noise in both conditions almost coincided because of their same airfoil trailing edge thickness, which further verifies the correctness of the simulation method. In addition, it is obvious that the TI noise also had little difference between the two conditions, which indicates that the slight turbulence in the WT wake does not cause obvious pressure fluctuations on the blade surface when it encounters the WT blades.

The wind speed comparison chart in Figure 14a is consistent with the comparison results in 8 m/s wind conditions. Wake interference increases the downstream turbulence, but due to the increase in wind speed, the wake turbulence is also compensated for to a certain extent, and the wind speed changes become smoother. The difference between the peaks and valleys is obtained by using the same analysis method as that below the rated wind speed of 8 m/s shown in Figure 16. It can be seen that the difference fluctuates significantly in the presence of wake interference, but the fluctuation becomes gentler, which further verifies that the influence of wake turbulence can be compensated for by increasing the inflow wind speed but not completely.

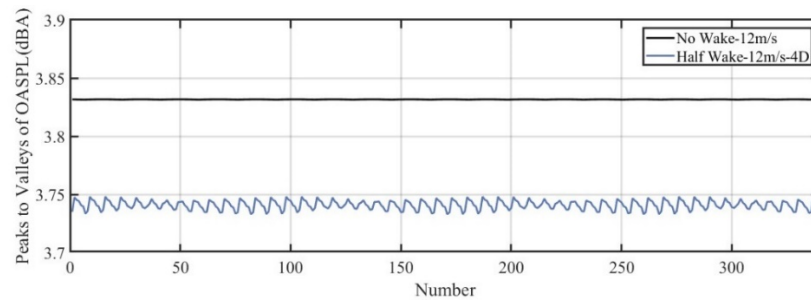


Figure 16. Comparison of peaks to valleys of OASPL with and without wake interference under 12 m/s steady wind conditions.

3.4. Influence of Wind Speed and Turbulence on OASPL Signals

In the actual atmospheric environment, steady wind is almost non-existent. To be more practical, the influence of turbulent wind on the aeroacoustic noise emission of a single WT in the wind farm is analyzed.

The turbulence intensity is set to 0.06, which is more suitable for offshore turbulence levels. Three turbulent average wind speeds at the hub position are shown in Figure 17. In Figure 18, it is obvious that, under the turbulent wind speed, the OASPL signals of the aerodynamic noise fluctuate significantly as a whole compared with the steady wind in Figure 8, indicating that the acoustic signal is sensitive to the turbulence to a certain extent; otherwise, the turbulence can be captured from the acoustic signals.

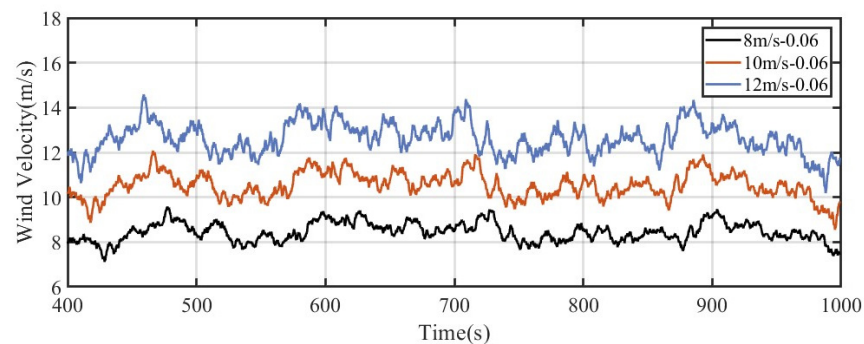


Figure 17. Schematic diagram of turbulent wind speed.

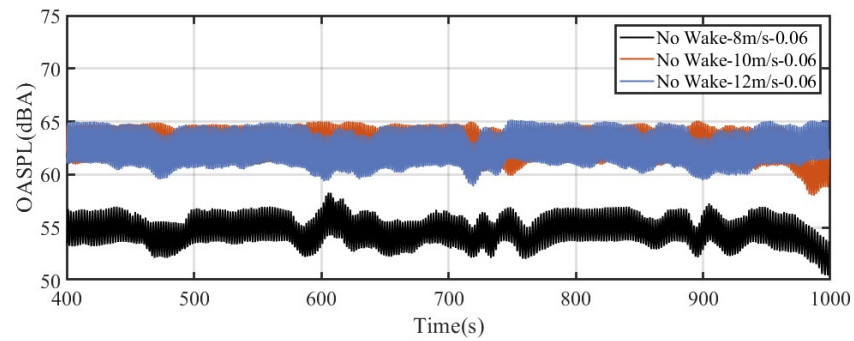


Figure 18. Schematic diagram of influence of different turbulent wind speeds on aeroacoustic noise emission of a single WT in wind farm.

It can be observed that, as the wind speed increases, the absolute value of the OASPL also increases before reaching the rated wind speed, which is in line with our understanding. Moreover, the absolute values of the OASPL are almost coincident under the conditions of 10 m/s and 12 m/s, which respectively approach and exceed the rated wind speed. So, only the 12 m/s wind speed is analyzed in the subsequent analysis, which is representative. When the wind speed is 8 m/s, the absolute value of the OASPL signal is significantly different from the other two wind speeds, which is also representative. Therefore, only two typical wind speeds below (8 m/s) and above (12 m/s) the rated wind speed are analyzed in the subsequent analysis.

3.5. Turbulent Wind Conditions

In this section, the correlation between wake interference and WT aerodynamic noise emission was preliminarily explored under steady wind conditions. This section selects the two wind speeds above for further exploration under turbulent wind conditions. Due to the influence of turbulence, the peaks-to-valleys method is no longer applicable, and new methods will be sought in this section.

With the contrast of the visualization schematic at steady wind conditions in Figures 7 and 12, the visualization of the turbulent inflow wind conditions in Figure 19 shows the wake meandering and more volatile wind speed. However, consistent with stationary operating, with the increase in the wind speed to 12 m/s, the wake-induced velocity deficit is effectively reduced, which is almost negligible.

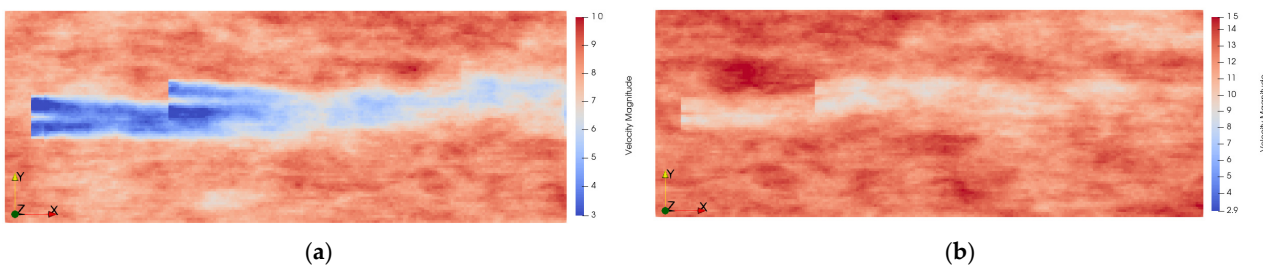


Figure 19. Visualization of wake under turbulent wind conditions: (a) 8 m/s; (b) 12 m/s.

3.5.1. Below Rated Wind Speed of 8 m/s

The OASPL signal measured by the microphone at each position shows the same variation trend in Figure 20. In the oblique direction of the WT (Observers 1, 3, 5, 7), the direct side direction of the WT (Observers 2, 6), the bottom of the tower (Observer 12), the front and rear of the WT (Observers 8, 4, 9,10), and above the hub (Observer 11), the OASPL signals show similar AMN characteristics. Although the OASPL measured by the microphones located at the front side of the WT and the base of the tower show strong AMN characteristics, the difference is not obvious, so it is not considered in the subsequent analysis. The signals measured by the microphones on the oblique side of the WT are

almost the same, so Observer 1 in the upwind direction is selected for the subsequent analysis. The acoustic signals measured by the other observers are almost the same, and Observer 4 located in the downwind direction is selected for the subsequent analysis.

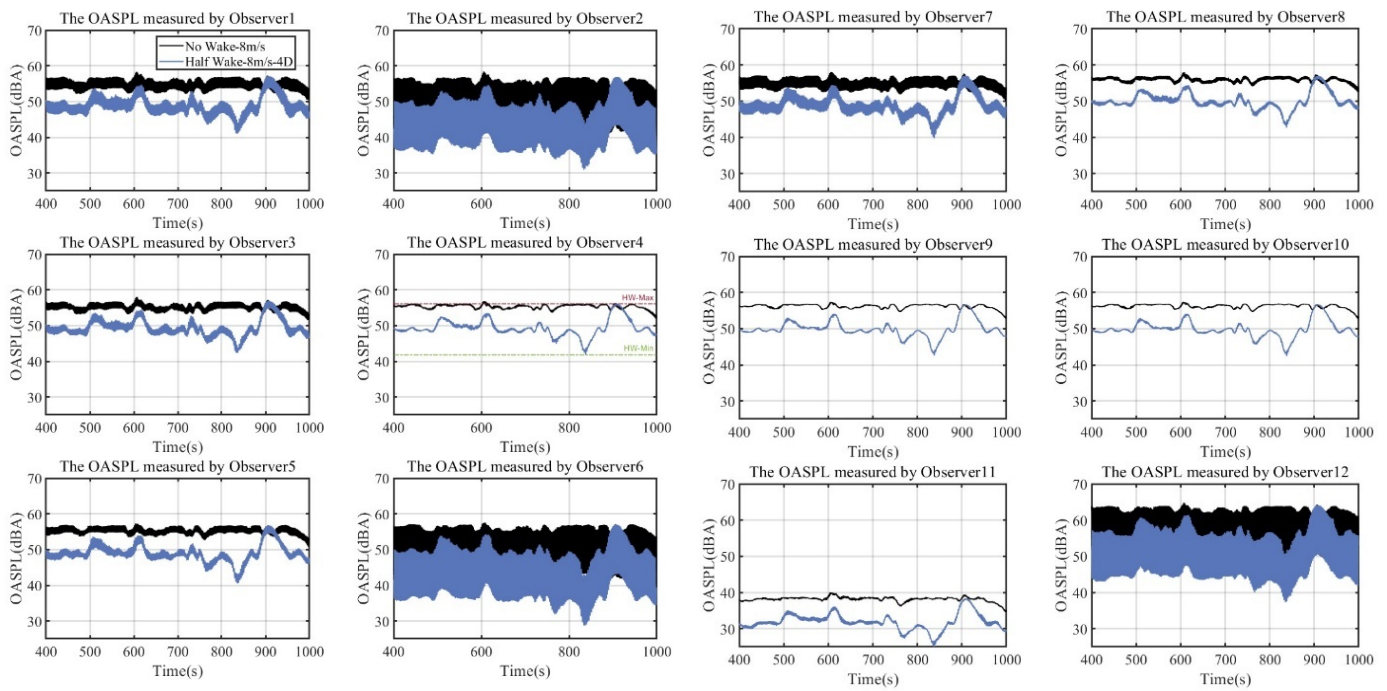


Figure 20. Schematic diagram for comparison of aeroacoustic noise time-domain SPL of WT measured at 12 microphone positions with and without wake effects under 8 m/s turbulent wind speed.

To further investigate the differences in the time-domain signals of aerodynamic noise from WT blades with and without wake interference, this paper calculates the differences between the mean values and the difference values between maximum and minimum values for each case. The results are respectively presented in Tables 5 and 6.

Table 5. The contrast in the absolute mean value of the OASPL.

Name	Mean Value of OASPL (NW) (dBA)	Mean Value of OASPL (NW) (dBA)	Augmentation (dBA)
Observer 1	54.65	48.82	5.83
Observer 2	46.52	40.89	5.63
Observer 3	55.16	49.41	5.75
Observer 4	55.32	49.34	5.98
Observer 5	55.22	48.90	6.32
Observer 6	46.65	40.15	6.50
Observer 7	54.74	48.68	6.06
Observer 8	55.91	50.04	5.87
Observer 9	56.15	49.95	6.20
Observer 10	56.19	49.90	6.29
Observer 11	38.14	31.88	6.26
Observer 12	57.82	51.80	6.02

Table 6. The contrast in the maximum and minimum difference values of the OASPL.

Observer Location	Difference Between Max and Min Value of OASPL (NW) (dBA)	Difference Between Max and Min Value of OASPL (HW) (dBA)	Augmentation (dBA)
Observer 1	7.82	16.07	8.25
Observer 2	18.17	26.03	7.86
Observer 3	6.43	14.55	8.12
Observer 4	4.92	14.23	9.31
Observer 5	6.53	16.19	9.66
Observer 6	17.97	28.20	10.23
Observer 7	8.11	17.29	9.18
Observer 8	5.48	14.29	8.81
Observer 9	4.60	14.07	9.47
Observer 10	4.71	14.18	9.47
Observer 11	5.44	13.36	7.92
Observer 12	18.46	26.79	8.33

From the time-domain results, the absolute value of the measured OASPL of the WT affected by the wake is reduced due to the wake deficit effect. The absolute value of the OASPL with wake interference is about 6 dBA lower than that without wake interference, as shown in Figure 21, which is consistent with the results under steady wind conditions. Moreover, the OASPL signals of the affected WT, in the entire analysis time domain, fluctuate over a wide range between the maximum and minimum limits, about 9 dBA more than that not affected by wake interference.

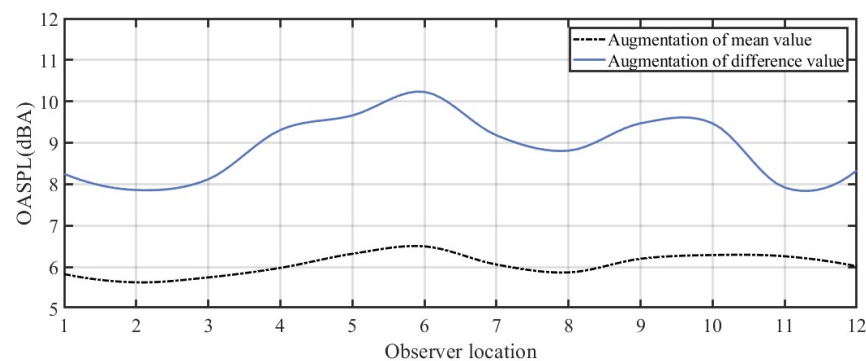


Figure 21. Schematic diagram of augmentation in mean value and difference between maximum and minimum value of OASPL under 8 m/s turbulent wind speed.

Another interesting result is that the augmentation in the difference between the maximum and minimum values of the OASPL shows a trend of increasing first and then decreasing from Observer 2 to Observer 1, as shown in Figure 21, and the largest augmentation value appeared in the direction of the downward sweep of the WT blades. In addition, Observers 4, 9, and 10 located in the same direction of the WT and the same distance from the WT tower are compared, and the difference is the same, which indicates that this parameter is closely related to the angular position of the observer around the WT. This also indicates that the downstream observer location is more sensitive to wake interference.

The results of the wind speed at this moment further verify the wind velocity deficit caused by the WT wake. At this time, when the WT suffers from a wake, its rotor speed, as shown in Figure 22b, is also significantly reduced, indirectly leading to the OASPL reduction. Moreover, the changing trend in the rotor speed is consistent with the trend in the OASPL, which indicates that the aeroacoustic noise signals are closely related to the rotor speed of the WT, and this conclusion is consistent with reference [39,44]. Although the DWM wake model often overestimates the wake deficit effects, they truly exist. To verify the relationship between the WT rotor speed and the OASPL, an amplitude spectrum

analysis of the OASPL in the time domain is carried out, and the results are shown in Figure 23.

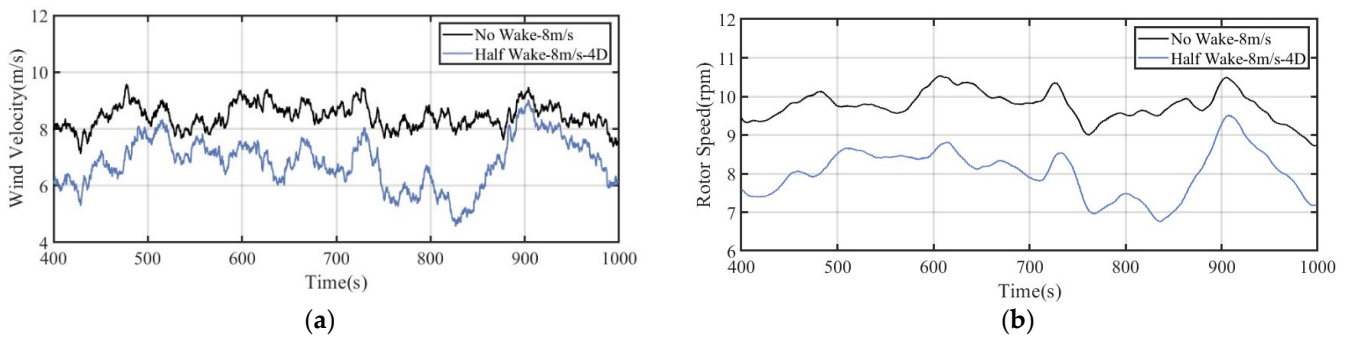


Figure 22. Schematic diagram of comparison between wake effects and non-wake effects under 8 m/s wind speed: (a) wind speed; (b) rotating speed.

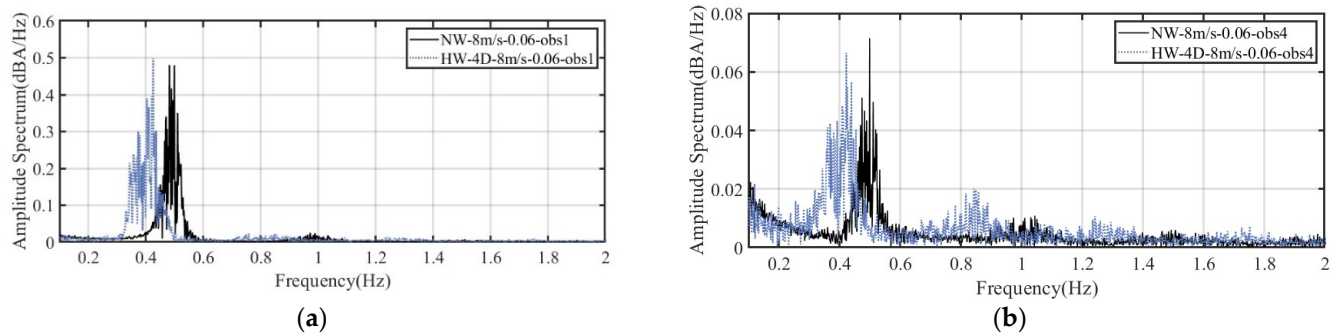


Figure 23. OASPL amplitude spectrum of WT with wake and without wake effects under 8m/s turbulent wind condition: (a) Observer 1; (b) Observer 4.

The BPF of the OASPL measured by Observers 1 and 4 is moved forward in the presence of wake interference, which shows a good corresponding relationship with the change in the rotor speed. In the presence of wake interference, the amplitude spectrum exhibits a wider band and more pronounced sub-peaks, which are more pronounced in the position of Observer 4. The reason for this is that the wake contains more turbulence. Furthermore, increases in the broadband components of two and three harmonics were evident downstream, while observer angles decreased marginally upstream. The reason for this phenomenon may be that the turbulent inflow causes loading noise, but this needs to be further verified.

To further validate wake turbulence, which is known to increase the fatigue loads of the downstream WT, the flapwise moment at the blade root of the WT with and without wake interference was analyzed, as shown in Figure 24.

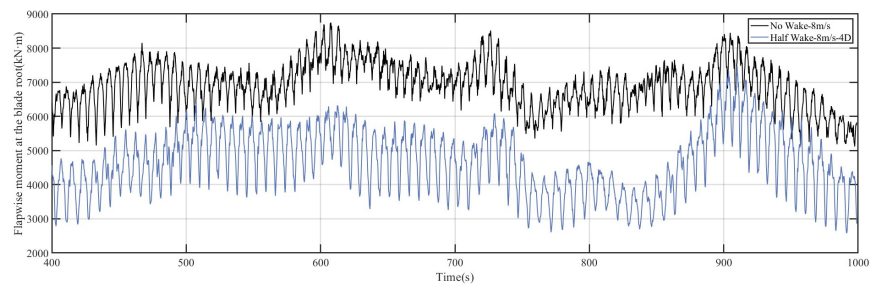


Figure 24. Flapwise moment at blade root of WT with and without wake effects under 8 m/s turbulent wind condition.

Although the absolute value of the blade root loads of the WT decreases under the effect of the wake, the fluctuation amplitude clearly increases, and the fatigue load increases, which verifies the existence of wake turbulence. The effect of wake turbulence is not captured in the time-domain OASPL signals; this is because the reduction in the absolute value of the OASPL signals caused by the wake deficit completely compensates for the increase in the OASPL signals caused by the wake turbulence. However, this potential effect of wake turbulence can be seen in the amplitude spectrum.

3.5.2. Above Rated Wind Speed of 12 m/s

Compared with the OASPL results at the 8 m/s wind speed, a comparison of the time-domain OASPL of the aeroacoustic noise of the WT above the rated wind speed of 12 m/s is harder to conduct because the increase in the wind speed compensates for 100% of the influence of the wake deficit effect and also partially compensates for the influence of the wake turbulence. According to the analysis of the results measured by the observers at 12 positions, the OASPL signals measured by Observers 4, 9, and 10 can more clearly show the increase in the absolute value of the OASPL caused by wake turbulence.

Compared to the results found in the three positions, Observers 1, 7, 3, and 5 show a large overlap in the OASPL results in Figure 25, so these positions are not advisable. And also, although the difference between the microphones at positions 9 and 10 seems to be more obvious, Observer 4 shows more obvious AMN characteristics, and considering the actual measurement environment and operation difficulty of the subsequent wake interference acoustic detection method, Observer 4 is selected for analysis. The total time results are shown in Figure 26.

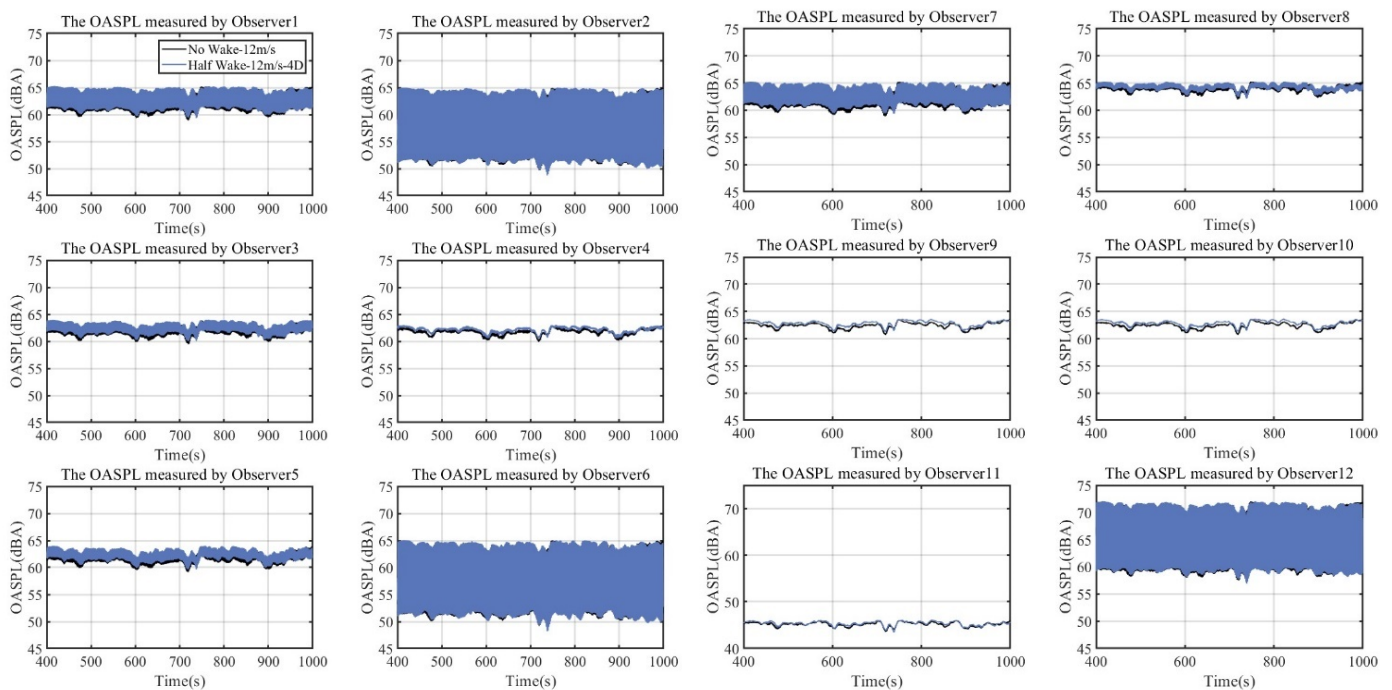


Figure 25. Schematic diagram for comparison of aeroacoustic noise time-domain SPL of WT measured at 12 microphone positions with and without wake effects under 12 m/s turbulent wind speed.

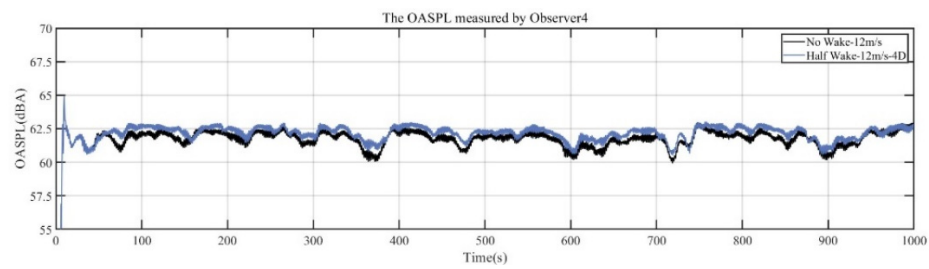


Figure 26. The OASPL of the WT in the time domain with and without wake interference under 12 m/s turbulent wind conditions at position 4.

It can be seen from Figure 26 that the absolute value of the OASPL of the WT with wake interference is larger than that of the WT without wake interference in the whole analysis time domain, but it can be seen from the wind speed diagram in Figure 27a that the wake interference causes a reduction in the downstream wind speed, which indicates that there is a wake deficit effect. The above analysis shows that the wake deficit will reduce the absolute value of the OASPL signal, but the simulation results are diametrically opposite. The OASPL value of the WT with wake interference is higher, indicating that the impact of wake turbulence exceeds the impact of wake deficit.

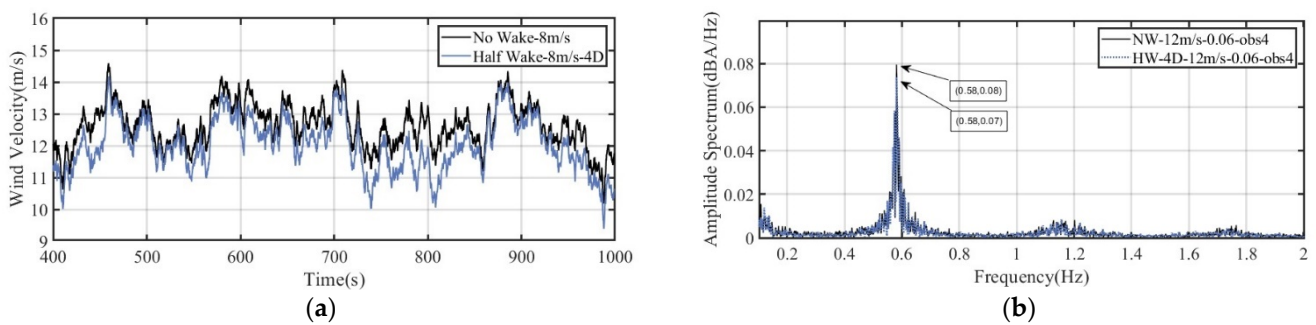


Figure 27. Schematic diagram of comparison of WT with and without wake effect at 12 m/s wind speed: (a) wind speed, (b) aeroacoustic noise amplitude spectrum.

In Figure 27b, the WT reached the rated wind speed at this time, and its speed is almost the same, so its BPF is almost coincident. Its frequency peak shows the same results as those in the steady wind condition. Still, its turbulence effect is not obvious in the amplitude spectrum, which further verifies that the wake turbulence effect is less obvious at high wind speeds than at low wind speeds, like steady wind conditions.

As with the analysis below the rated wind speed of 8 m/s, the load of the blade root was also analyzed to verify the presence of turbulence.

In wake interference, the absolute value of the blade root loads increases. To make the results more obvious, Savitzky–Golay smoothing filtering is performed, and the filtering is performed for every 250 data points. The results are shown as the solid line in Figure 28, from which it can be observed that the blade root loads increase significantly. It further verifies the existence of turbulence information in the wake flow, which also supports the fact that the downstream wind velocity deficit caused by the wake is compensated for, and the wake turbulence is revealed.

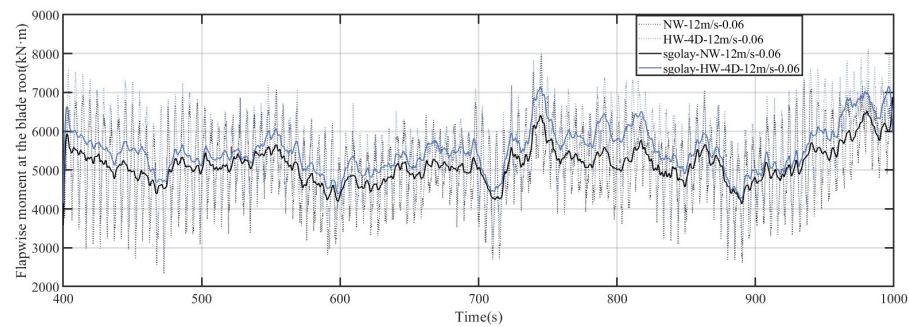


Figure 28. The flapwise moment at the blade root of the WT with and without wake effects under the 12 m/s turbulent wind condition.

4. Discussion and Conclusions

This paper examines the influence of wake deficit and wake turbulence on the aeroacoustic noise emission of WTs. Based on the verification of the AM characteristics of the simulation results, a preliminary analysis is conducted under steady wind conditions, with further exploration under turbulent wind conditions. The OASPL results are analyzed in conjunction with various outputs of the WT, focusing on two main aspects: the time domain and the frequency domain.

The conclusions of this paper are summarized in the following five points:

1. The WT wake will affect the aeroacoustic noise emission of the downstream WT, which can be reflected in the acoustic signals. Hence, the acoustic detection method of wake interference is feasible.
2. The influence of the wake deficit effect on OASPL signals is dominant at 8 m/s. Thus, the influence of wake turbulence is dominant at 12 m/s. These effects are expressed in the absolute value of the OASPL in the time domain. The wake deficit will reduce the downstream wind speed, which will reduce the rotor speed of the WT and indirectly reduce the absolute value of the OASPL by about 6 dBA, while the wake turbulence will increase it marginally.
3. Wake turbulence will cause larger fluctuations in the OASPL. Compared with the WT that is not affected by wake interference, the OASPL of the affected WT fluctuates within about 9 dBA larger maximum and minimum limits, which is more obvious at 8 m/s. However, such influence will be weakened by the increase in wind speed.
4. In the frequency domain, the wake interference will make the spectrum of the OASPL have a wider frequency band and will show more obvious sub-peaks at 8 m/s. Wake interference will reduce tip vortex noise emission so that the OASPL spectrum's frequency peak will be reduced to 12 m/s.
5. If the acoustic method is used for wake interference detection in the future, it is recommended to place the microphone at the position of Observer 4. The distance from the lower part of the tower and its calculation will be according to the IEC61400-11 standard. Based on the work in this paper, it is found that the microphone at this position is more sensitive to wake interference. Furthermore, the wake interference acoustic detection method is recommended at low wind speeds.

5. Limitations and Perspectives

The limitations and perspectives of this paper are summarized in the following three points:

1. The wake model used in this paper is of medium fidelity, while the TI noise is low-frequency. The model used in this paper does not present the calculation results well, so the results obtained may deviate from the actual situation. A higher-fidelity wake model and more precise TI noise calculation model can be used for related research in the future.

2. In all simulations, the wake meandering setting is left as default as the official one, and the effects of turbulence intensity and wind shear index will be studied later.
3. In this paper, the analysis objects are all A-weighted OASPLs, and the non-A-weighted OASPL and the differences between the two parameters will be explored in a future study.

Author Contributions: Conceptualization, Y.Y. and Y.X.; methodology, Y.Y. and L.X.; formal analysis, Y.Y.; data curation, Y.Y.; writing—original draft preparation, Y.Y.; writing—review and editing, Y.Y., L.X., J.W. and Y.X.; visualization, Y.Y., J.W. and Z.Y.; funding acquisition, Y.X. All authors have read and agreed to the published version of the manuscript.

Funding: This research was funded by Shandong Provincial Natural Science Foundation, grant number ZR2021ZD23. This research was also funded by the Offshore Wind Power Intelligent Measurement and Control Research Centre and Laboratory Construction at the Ocean University of China, grant number 861901013159.

Institutional Review Board Statement: Not applicable.

Informed Consent Statement: Not applicable.

Data Availability Statement: The data presented in this study are available on request from the corresponding author. The data are not publicly available due to their containing information that could compromise the privacy of research participants.

Acknowledgments: We wish to thank Jonkman Jason of National Renewable Energy Laboratory.

Conflicts of Interest: The authors declare that they have no known competing financial interests or personal relationships that could have appeared to influence the work reported in this paper.

References

1. Bayron, P.; Kelso, R.; Chin, R. Experimental analysis of co-rotating and counter-rotating tandem horizontal-axis wind turbine performance and wake dynamics. *J. Wind Eng. Ind. Aerodyn.* **2024**, *253*, 105840. [[CrossRef](#)]
2. Sergiienko, N.Y.; da Silva, L.S.P.; Bachynski-Polić, E.E.; Cazzolato, B.S.; Arjomandi, M.; Ding, B. Review of scaling laws applied to floating offshore wind turbines. *Renew. Sustain. Energy Rev.* **2022**, *162*, 112477. [[CrossRef](#)]
3. Alex. *Global Wind Report 2024*; Global Wind Energy Council: Singapore, 2024.
4. Ata Teneler, A.; Hassoy, H. Health effects of wind turbines: A review of the literature between 2010–2020. *Int. J. Environ. Health Res.* **2023**, *33*, 143–157. [[CrossRef](#)]
5. Cheng, Z.; Lien, F.-S.; Yee, E.; Meng, H. A unified framework for aeroacoustics simulation of wind turbines. *Renew. Energy* **2022**, *188*, 299–319. [[CrossRef](#)]
6. Thomsen, F.; Stöber, U.; Sarnocińska-Kot, J. Hearing Impact on Marine Mammals Due to Underwater Sound from Future Wind Farms. In *The Effects of Noise on Aquatic Life: Principles and Practical Considerations*; Popper, A.N., Sisneros, J., Hawkins, A.D., Thomsen, F., Eds.; Springer International Publishing: Cham, Switzerland, 2023; pp. 1–7.
7. Siddagangaiah, S.; Chen, C.F.; Hu, W.-C.; Akamatsu, T.; Pieretti, N. Assessing the influence of offshore wind turbine noise on seasonal fish chorusing. *ICES J. Mar. Sci.* **2024**, *0*, fsae061. [[CrossRef](#)]
8. Ishihara, T.; Qian, G.-W. A new Gaussian-based analytical wake model for wind turbines considering ambient turbulence intensities and thrust coefficient effects. *J. Wind Eng. Ind. Aerodyn.* **2018**, *177*, 275–292. [[CrossRef](#)]
9. Chen, G.; Li, X.-B.; Liang, X.-F. IDDES simulation of the performance and wake dynamics of the wind turbines under different turbulent inflow conditions. *Energy* **2022**, *238*, 121772. [[CrossRef](#)]
10. Xue, L.; Wang, J.; Zhao, L.; Wei, Z.; Yu, M.; Xue, Y. Wake Interactions of Two Tandem Semisubmersible Floating Offshore Wind Turbines Based on FAST.Farm. *J. Mar. Sci. Eng.* **2022**, *10*, 1962. [[CrossRef](#)]
11. Kuang, L.; Katsuchi, H.; Zhou, D.; Chen, Y.; Han, Z.; Zhang, K.; Wang, J.; Bao, Y.; Cao, Y.; Liu, Y. Strategy for mitigating wake interference between offshore vertical-axis wind turbines: Evaluation of vertically staggered arrangement. *Appl. Energy* **2023**, *351*, 121850. [[CrossRef](#)]
12. Barthelmie, R.J.; Hansen, K.S.; Pryor, S.C. Meteorological Controls on Wind Turbine Wakes. *Proc. IEEE* **2013**, *101*, 1010–1019. [[CrossRef](#)]
13. Zhao, L.; Gong, F.; Chen, S.; Wang, J.; Xue, L.; Xue, Y. Optimization study of control strategy for combined multi-wind turbines energy production and loads during wake effects. *Energy Rep.* **2022**, *8*, 1098–1107. [[CrossRef](#)]
14. Zhao, L.; Gong, Y.; Gong, F.; Zheng, B.; Wang, J.; Xue, L.; Xue, Y. Study on Mitigation of Wake Interference by Combined Control of Yaw Misalignment and Pitch. *J. Mar. Sci. Eng.* **2023**, *11*, 1288. [[CrossRef](#)]
15. Rotta, J. *On the Theory of the Turbulent Boundary Layer*; NASA: Washington, DC, USA, 1953.
16. Clauser, F.H. The Turbulent Boundary Layer. *Adv. Appl. Mech.* **1956**, *4*, 1–51.

17. Coull, J.D.; Hodson, H.P. Unsteady boundary-layer transition in low-pressure turbines. *J. Fluid Mech.* **2011**, *681*, 370–410. [CrossRef]
18. Harun, Z.; Monty, J.P.; Mathis, R.; Marusic, I. Pressure gradient effects on the large-scale structure of turbulent boundary layers. *J. Fluid Mech.* **2013**, *715*, 477–498. [CrossRef]
19. Sajadmanesh, S.M.; Mohseni, A.; Mojaddam, M. Vortex dynamics mechanisms of separated boundary layer in a highly loaded low pressure turbine cascade. *Int. J. Heat Fluid Flow* **2020**, *82*, 108540. [CrossRef]
20. Goldstein, M.E. *Aeroacoustics*; McGraw Hill: New York, NY, USA, 1976.
21. Lilley, G. On the Noise from Jets. 1974. Available online: <https://pascal-francis.inist.fr/vibad/index.php?action=getRecordDetail&idt=PASCAL7530050182> (accessed on 12 September 2024).
22. Lee, S.; Ayton, L.; Bertagnolio, F.; Moreau, S.; Chong, T.P.; Joseph, P. Turbulent boundary layer trailing-edge noise: Theory computation, experiment, and application. *Prog. Aerosp. Sci.* **2021**, *126*, 100737. [CrossRef]
23. Amiri, M.M.; Shadman, M.; Estefen, S.F. A review of physical and numerical modeling techniques for horizontal-axis wind turbine wakes. *Renew. Sustain. Energy Rev.* **2024**, *193*, 114279. [CrossRef]
24. *IEEE Std 2400-2016*; IEEE Standard for Wind Turbine Aero Acoustic Noise Measurement Techniques. IEEE: Piscataway Township, NJ, USA, 2016; pp. 1–24. [CrossRef]
25. Kim, J.; Haeri, S.; Joseph, P. On the reduction of aerofoil–turbulence interaction noise associated with wavy leading edges. *J. Fluid Mech.* **2016**, *792*, 526–552. [CrossRef]
26. Jiang, M.; Li, X.; Bai, B.; Lin, D. Numerical simulation on the NACA0018 airfoil self-noise generation. *Theor. Appl. Mech. Lett.* **2012**, *2*, 052004. [CrossRef]
27. Amiet, R.K. Acoustic radiation from an airfoil in a turbulent stream. *J. Sound Vib.* **1975**, *41*, 407–420. [CrossRef]
28. Brooks, T.F.; Pope, D.S.; Marcolini, M.A. *Airfoil Self-Noise and Prediction*; NASA: Washington, DC, USA, 1989.
29. Wang, H.; Chen, B. Investigation on aerodynamic noise for leading edge erosion of wind turbine blade. *J. Wind Eng. Ind. Aerodyn.* **2023**, *240*, 105484. [CrossRef]
30. Wang, W.; Yan, Y.; Zhao, Y.; Xue, Y. Studies on the Experimental Measurement of the Low-Frequency Aerodynamic Noise of Large Wind Turbines. *Energies* **2024**, *17*, 1609. [CrossRef]
31. Abdelsalam, A.M.; El-Shorbagy, M.A. Optimization of wind turbines siting in a wind farm using genetic algorithm based local search. *Renew. Energy* **2018**, *123*, 748–755. [CrossRef]
32. Parchen, R.R. *Progress Report DRAW: A Prediction Scheme for Trailing Edge Noise Based on Detailed Boundary Layer Characteristics*; TNO Institute of Applied Physics: Delft, The Netherlands, 1998.
33. Paterson, R.; Amiet, R. Acoustic radiation and surface pressure characteristics of an airfoil due to incident turbulence. In Proceedings of the 3rd Aeroacoustics Conference, Palo Alto, CA, USA, 20–23 July 1976; American Institute of Aeronautics and Astronautics: Reston, VA, USA, 1976.
34. Guidati, G.; Bareiss, R.; Wagner, S.; Parchen, R.; Guidati, G.; Bareiss, R.; Wagner, S.; Parchen, R. Simulation and measurement of inflow-turbulence noise on airfoils. In Proceedings of the 3rd AIAA/CEAS Aeroacoustics Conference, Aeroacoustics Conferences, Atlanta, GA, USA, 12–14 May 1997; American Institute of Aeronautics and Astronautics: Reston, VA, USA, 1997.
35. Moriarty, P.; Migliore, P. *Semi-Empirical Aeroacoustic Noise Prediction Code for Wind Turbines*; NREL/TP-500-34478; National Renewable Energy Laboratory: Golden, CO, USA, 2003; p. 15006098.
36. Zhao, L.; Xue, L.; Li, Z.; Wang, J.; Yang, Z.; Xue, Y. Progress on Offshore Wind Farm Dynamic Wake Management for Energy. *J. Mar. Sci. Eng.* **2022**, *10*, 1395. [CrossRef]
37. Churchfield, M.J.; Lee, S.; Moriarty, P.J.; Hao, Y.; Lackner, M.A.; Barthelmie, R.; Lundquist, J.K.; Oxley, G. A Comparison of the Dynamic Wake Meandering Model, Large-Eddy Simulation, and Field Data at the Egmond aan Zee Offshore Wind Plant. In *33rd Wind Energy Symposium*; American Institute of Aeronautics and Astronautics: Reston, VA, USA, 2015.
38. Larsen, G.C.; Madsen Aagaard, H.; Bingöl, F.; Mann, J.; Ott, S.; Sørensen, J.N.; Okulov, V.; Troldborg, N.; Nielsen, N.M.; Thomsen, K.; et al. *Dynamic Wake Meandering Modeling*; Risø National Laboratory: Roskilde, Denmark, 2007; ISBN 978-87-550-3602-4.
39. Petricelli, F.; Chaitanya, P.; Palleja-Cabre, S.; Meloni, S.; Joseph, P.F.; Karimian, A.; Palani, S.; Camussi, R. An experimental investigation on the effect of in-flow distortions of propeller noise. *Appl. Acoust.* **2023**, *214*, 109682. [CrossRef]
40. Celik, A.; Syafiqah Jamaluddin, N.; Baskaran, K.; Meloni, S.; Rezgui, D.; Azarpeyvand, M. Experimental characterisation of rotor noise in tandem configuration. *Appl. Acoust.* **2024**, *222*, 110053. [CrossRef]
41. Zaman, I.; Falsi, M.; Zang, B.; Azarpeyvand, M.; Meloni, S. On the aeroacoustics of turbulent boundary layer ingesting propellers. *Phys. Fluids* **2024**, *36*, 075172. [CrossRef]
42. Heimann, D.; Käsler, Y.; Gross, G. The wake of a wind turbine and its influence on sound propagation. *Meteorol. Z.* **2011**, *20*, 449–460. [CrossRef]
43. Barlas, E.; Zhu, W.J.; Shen, W.Z.; Kelly, M.; Andersen, S.J. Effects of wind turbine wake on atmospheric sound propagation. *Appl. Acoust.* **2017**, *122*, 51–61. [CrossRef]
44. Bertagnolio, F.; Aa Madsen, H.; Fischer, A. Noise emission from wind turbines in wake - Measurement and modeling: The Science of Making Torque from Wind 2018. *J. Phys. Conf. Ser.* **2018**, *1037*, 022001. [CrossRef]
45. Jonkman, J.; Shaler, K. *FAST.Farm User's Guide and Theory Manual*; National Renewable Energy Laboratory: Golden, CO, USA, 2021.

46. National Renewable Energy Laboratory. *OpenFAST Documentation—OpenFAST v3.5.3 Documentation*; National Renewable Energy Laboratory: Golden, CO, USA, 2023.
47. Bortolotti, P.; Tarres, H.C.; Dykes, K.L.; Merz, K.; Sethuraman, L.; Verelst, D.; Zahle, F. *IEA Wind TCP Task 37: Systems Engineering in Wind Energy-WP2.1 Reference Wind Turbines*; NREL/TP-5000-73492; National Renewable Energy Laboratory: Golden, CO, USA, 2019.
48. Bortolotti, P.; Branlard, E.; Platt, A.; Moriarty, P.; Sucameli, C.; Bottasso, C. *Aeroacoustics Noise Model of OpenFAST*; NREL/TP-5000-75731; National Renewable Energy Laboratory: Golden, CO, USA, 2020; p. 1660130.
49. Moriarty, P.; Guidati, G.; Migliore, P. Recent Improvement of a Semi-Empirical Aeroacoustic Prediction Code for Wind Turbines. In *Proceedings of the 10th AIAA/CEAS Aeroacoustics Conference, Aeroacoustics Conferences, Manchester, UK, 10–12 May 2004*; American Institute of Aeronautics and Astronautics: Reston, VA, USA, 2004.
50. Zhu, W.J.; Heilskov, N.; Shen, W.Z.; Sørensen, J.N. Modeling of Aerodynamically Generated Noise From Wind Turbines. *J. Sol. Energy Eng.* **2005**, *127*, 517–528. [[CrossRef](#)]
51. Moriarty, P.; Guidati, G.; Migliore, P. Prediction of Turbulent Inflow and Trailing-Edge Noise for Wind Turbines. In *Proceedings of the 11th AIAA/CEAS Aeroacoustics Conference, Monterey, CA, USA, 23–25 May 2005*; Aeroacoustics Conferences. American Institute of Aeronautics and Astronautics: Reston, VA, USA, 2005.
52. Jonkman, B.J. *TurbSim User's Guide*; NREL/TP-500-39797; National Renewable Energy Laboratory: Golden, CO, USA, 2006.
53. *IEC 61400-3; Wind Turbines—Part 3: Design Requirements for Offshore Wind Turbines*. GlobalSpec: Albany, NY, USA, 2019.
54. *IEC 61400-11; Wind Turbines—Part 11: Acoustic Noise Measurement Techniques*. EIRIE: Springfield, OH, USA, 2012.

Disclaimer/Publisher's Note: The statements, opinions and data contained in all publications are solely those of the individual author(s) and contributor(s) and not of MDPI and/or the editor(s). MDPI and/or the editor(s) disclaim responsibility for any injury to people or property resulting from any ideas, methods, instructions or products referred to in the content.